Published August 16, 2010

Clathrin-independent carriers form a high capacity endocytic sorting system at the leading edge of migrating cells

Mark T. Howes,[1,2] Matthew Kirkham,[1] James Riches,[2] Katia Cortese,[1,2] Piers J. Walser,[1] Fiona Simpson,[1] Michelle M. Hill,[1] Alun Jones,[1] Richard Lundmark,[3] Margaret R. Lindsay,[1,2] Delia J. Hernandez-Deviez,[1] Gordana Hadzic,[4] Adam McCluskey,[4] Rumasia Bashir,[5] Libin Liu,[6] Paul Pilch,[6] Harvey McMahon,[3] Phillip J. Robinson,[7] John F. Hancock,[1] Satyajit Mayor,[8] and Robert G. Parton[1,2]

[1]The Institute for Molecular Bioscience and [2]The Centre for Microscopy and Microanalysis, The University of Queensland, Brisbane, Queensland 4072, Australia
[3]MRC Laboratory of Molecular Biology, Cambridge CB2 0QH, England, UK
[4]Chemistry, School of Environmental and Life Sciences, The University of Newcastle, Callaghan, NSW 2308, Australia
[5]School of Biological and Biomedical Sciences, Durham University, Durham DH1 3HP, England, UK
[6]Department of Biochemistry, Boston University School of Medicine, Boston, MA 02118
[7]Children's Medical Research Institute, The University of Sydney, Sydney, NSW 2145, Australia
[8]National Centre for Biological Science (TIFR), Bangalore 560 065, India

Although the importance of clathrin- and caveolin-independent endocytic pathways has recently emerged, key aspects of these routes remain unknown. Using quantitative ultrastructural approaches, we show that clathrin-independent carriers (CLICs) account for approximately three times the volume internalized by the clathrin-mediated endocytic pathway, forming the major pathway involved in uptake of fluid and bulk membrane in fibroblasts. Electron tomographic analysis of the 3D morphology of the earliest carriers shows that they are multidomain organelles that form a complex sorting station as they mature. Proteomic analysis provides direct links between CLICs, cellular adhesion turnover, and migration. Consistent with this, CLIC-mediated endocytosis of key cargo proteins, CD44 and Thy-1, is polarized at the leading edge of migrating fibroblasts, while transient ablation of CLICs impairs their ability to migrate. These studies provide the first quantitative ultrastructural analysis and molecular characterization of the major endocytic pathway in fibroblasts, a pathway that provides rapid membrane turnover at the leading edge of migrating cells.

Introduction

Endocytosis provides a crucial and dynamic interface between the extracellular milieu and the interior of the cell. This interface is paramount for fluid and nutrient uptake, signaling regulation, lipid homeostasis, plasma membrane (PM) remodeling, synaptic vesicle recycling, and cellular motility (Grande-García et al., 2007; Mayor and Pagano, 2007; Idone et al., 2008b; Sigismund et al., 2008). Correspondingly, the endocytic system entails a rich diversity of mechanisms coordinated across several pathways. Mounting evidence suggests that eukaryotic cells maintain up to five distinct, constitutive pinocytic pathways (excluding

Correspondence to Robert G. Parton: r.parton@imb.uq.edu.au

M. Kirkham's present address is Department of Cell and Molecular Biology, Karolinska Institute, 17177 Stockholm, Sweden.

J. Riches' present address is European Molecular Biology Laboratory, Meyerhofstrasse 1, 69117 Heidelberg, Germany.

K. Cortese's present address is Centro di Ricerca MicroSCoBio/IFOM, FIRC Institute of Molecular Oncology, Università di Genova, 16126 Genova, Italy.

F. Simpson's and M.M. Hill's present address is The University of Queensland, Diamentina Institute for Cancer, Immunology and Metabolic Medicine, Brisbane, Queeensland 4102, Australia.

R. Lundmark's present address is Department of Medical Biochemistry and Biophysics, Umeå University, 901 87 Umeå, Sweden.

Abbreviations used in this paper: AA, ascorbic acid; CIE, clathrin-independent endocytosis; CLIC, clathrin-independent carrier; CME, clathrin-mediated endocytosis; CTxB, cholera toxin B subunit; GPI-AP, glycosylphosphatidylinositol-anchored protein; MEF, mouse embryonic fibroblast; PM, plasma membrane; RE, recycling endosome; Tf, transferrin; WT, wild type.

Supplemental Material can be found at:
http://jcb.rupress.org/content/suppl/2010/08/16/jcb.201002119.DC1.html
Original image data can be found at:
http://jcb-dataviewer.rupress.org/jcb/browse/2556

The Rockefeller University Press $30.00
J. Cell Biol. Vol. 190 No. 4 675–691
www.jcb.org/cgi/doi/10.1083/jcb.201002119

Published August 16, 2010

phagocytosis and macropinocytosis; Doherty and McMahon, 2009). These are clathrin-mediated endocytosis (CME), caveolae, and three noncaveolar clathrin-independent endocytic (CIE) routes, which are defined based on specific regulation by RhoA (Lamaze et al., 2001), Arf6 (Radhakrishna and Donaldson, 1997), or Cdc42 (Sabharanjak et al., 2002). Many of the cargo and regulators of the classical CME and caveolae pathways have been identified and the dynamics of these pathways are the best understood (for reviews see Conner and Schmid, 2003; Parton and Simons, 2007). Comparatively, very little is known about the mechanisms governing CIE, although recent work has emphasized the crucial importance of these pathways (Mayor and Pagano, 2007).

The existence of CIE pathways was first proposed from the study of plant and bacterial toxin internalization, in combination with ultrastructural methods or with tools that inhibited CME (Montesano et al., 1982; Sandvig et al., 1987; Ricci et al., 2000). The plant toxin ricin was used to first describe the clathrin-independent, apical endocytic pathway in endothelial cells (Sandvig and van Deurs, 1994). Bacterial toxins, such as the *Helicobacter pylori* VacA toxin (Gauthier et al., 2007) and cholera toxin (Torgersen et al., 2001) provided further evidence for clathrin-independent endocytic pathways. However, a lack of specific tools to study these noncanonical routes has made it difficult to identify their guiding parameters.

Ultrastructural work on the CIE pathway regulated by Cdc42 has identified the morphologically distinct clathrin-independent carriers (CLICs) as the primary carriers involved in uptake within this route (Kirkham et al., 2005). Parameters currently identified for the CLIC pathway include dynamin-independent PM scission (Sabharanjak et al., 2002), enrichment in GPI-anchored proteins (Sabharanjak et al., 2002), reliance on Arf1 activity (Sabharanjak et al., 2002; Kumari and Mayor, 2008), sensitivity to cholesterol depletion (Kirkham et al., 2005; Chadda et al., 2007), and contribution to a significant fraction of cholera toxin B subunit (CTxB) and fluid internalization (Kirkham et al., 2005). CLICs arise directly from the PM and mature into the GPI-enriched early endosomal compartment (GEEC), as they acquire Rab5 and EEA-1 and, consequently, merge with early endosomes (EEs; Kalia et al., 2006). Ongoing work is linking cargo and regulators to these carriers, such as GTPase regulator associated with FAK (GRAF1), dysferlin, and Snx9 (Yarar et al., 2007; Hernández-Deviez et al., 2008; Lundmark et al., 2008). The basic parameters of these carriers, however, remain unknown.

Here we characterize key parameters of the CLIC pathway. A quantitative analysis of the volume and surface area of CLICs identifies them as the major constitutive pathway involved in bulk endocytosis within fibroblasts. High resolution electron tomography shows the complexity of these primary endocytic carriers and, in conjunction with recruitment of classical trafficking regulators, they are realized to be intricate sorting compartments. Identification of novel CLIC cargo suggests links to cellular adhesion turnover and plasma membrane repair. Consistent with this, CLICs become polarized in migrating fibroblasts, turning over adhesion complex components, such as Thy-1 and CD44, at the leading edge. Inhibition of the CLIC pathway subsequently impairs the capacity of fibroblasts to migrate.

Results

CLICs account for the major constitutive uptake of fluid and bulk membrane in fibroblasts

Quantitation of the volume and surface area internalizing through the CLIC pathway is vital for understanding the contribution of this route to total endocytosis and PM homeostasis. Generic endocytic markers that enter via CME, caveolae, and CIE routes, such as HRP or CTxB, have been used in conjunction with ultrastructural morphology and dynamin independence to define CLICs (Kirkham et al., 2005). Therefore, we first used HRP-conjugated CTxB (CTxB-HRP) as an endocytic membrane marker with a previously characterized diaminobenzidine (DAB) incubation protocol for EM visualization (Kirkham et al., 2005). This method reveals only internalized carriers and can be used to label such carriers within seconds of scission. Although CTxB-HRP is an excellent membrane marker, a multivalent toxin could theoretically affect endocytosis, particularly when combined with an incubation step at low temperature (Römer et al., 2007). Therefore, quantitative measurements of the very early uptake of the fluid phase marker, HRP (at 20 $mg.ml^{-1}$), were compared with CTxB-HRP and assessed in the presence or absence of unlabeled CTxB (Fig. 1, A and B) to determine the relative contribution of CME and CLICs in both wild-type (WT) and caveolin1-null ($Cav1^{-/-}$) mouse embryonic fibroblasts (MEFs). These experiments allowed us to eliminate a cold step and showed that HRP and CTxB-HRP labeled identical compartments, whereas CTxB did not quantitatively affect endocytosis (Fig. 1, C–E).

A defining characteristic of the CLIC pathway is independence of dynamin for PM scission (Damke et al., 1994; Parton et al., 1994; Henley et al., 1998; Lamaze et al., 2001; Pelkmans et al., 2002; Sabharanjak et al., 2002; Kirkham et al., 2005). Therefore, we used a well-characterized small molecule inhibitor of dynamin, dynasore (unpublished data), as well as a more potent, hydroxylated analogue of dynasore, Dyngo4a (unpublished data) to inhibit CME, caveolar endocytosis, and dynamin-dependent CIE pathways. The activity of these inhibitors in WT and $Cav1^{-/-}$ MEFs was confirmed by assessing the fluorescence uptake of the CME cargo protein transferrin (Tf-647) and the generic endocytic marker CTxB-555 (Fig. 1 F), as well as visualization of CTxB-HRP–labeled carriers by EM (Fig. 1 G). Although Tf-647 and CTxB-555 were both efficiently internalized in untreated control cells, after treatment with 30 μM Dyngo4a (or 80 μM dynasore) only CTxB-555 internalization occurred. In agreement with this observation, in untreated control cells, CTxB-HRP labeling was found in both CLICs (Fig. 1 G, arrows) and clathrin-coated vesicles (CCVs; Fig. 1 G, double arrowheads), visualized by EM. However, in the presence of Dyngo4a, only CLICs, defined by ultrastructure, were active (Fig. 1 G, arrows). Unlabeled clathrin-coated pits (CCPs) were readily observed but were surface connected (Fig. 1 G, arrowheads). Together, these data show that CTxB is a useful marker for CLICs and, when combined with acute dynamin inhibition using Dyngo4a, CLICs remain the only detectably active endocytic pathway.

Published August 16, 2010

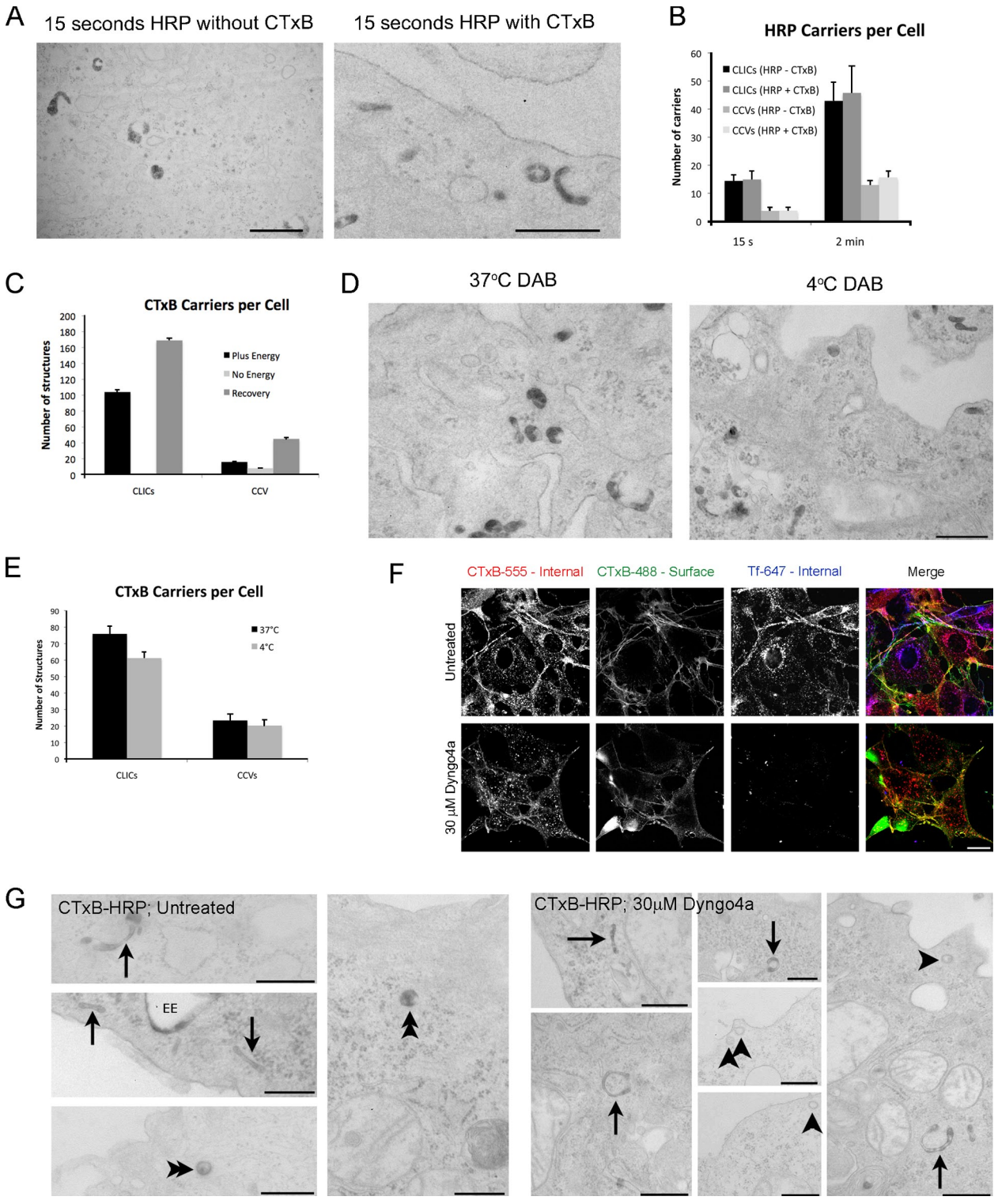

Figure 1. **CTxB does not affect CLIC endocytosis.** (A) Cav1$^{-/-}$ MEFs were incubated with HRP in the presence or absence of CTxB for 15 s. Cells were cooled and DAB reaction perfomed in the presence of ascorbic acid (AA) before fixation. Bars, 200 nm. (B) Quantitation of the number of HRP-filled carriers per cell across 10–12 cells treated as in A. CLICs were defined by their characteristic ring-shaped morphology, CCVs were defined as coated vesicular carriers. Error bars show SEM. (C) Cav1$^{-/-}$ MEFs were grown in normal media (plus energy), media containing 2-deoxyglucose (no energy), or 2-deoxyglucose media for 1 h followed by a 1-h washout in normal media (recovery) before CTxB-HRP internalization and DAB reaction. Labeled structures were counted across 10 cells. Error bars show SEM. (D and E) Cav1$^{-/-}$ MEFs were incubated with CTxB-HRP for 5 min before the DAB reaction for either 5 min at 37°C or 10 min at 4°C, followed by fixation at 37°C. All CTxB-HRP–positive structures were counted in 10–12 cells across two independent experiments. Error bars show SEM. Bar, 200 nm. (F) NIH3T3s were treated for 20 min with vehicle (Untreated) or Dyngo4a before internalization of CTxB-555 (left panels) and Tf-647 (right panels) for 5 min. Cells were placed on ice and acid stripped to remove surface labeling. Cells were then bound with CTxB-488 (middle panels). Bar, 10 μm. (G) NIH3T3 cells were left untreated or were treated with Dyngo4a before internalization of CTxB-HRP, followed by DAB reaction. Arrows show CTxB-HRP–laden CLICs, double arrowheads show internalized, labeled CCVs, arrowheads show surface connected unlabeled CCPs. Bars, 200 nm.

Published August 16, 2010

Having established the constitutive nature of the pathway and lack of detectable perturbation by the used markers, we used EM-based stereology to calculate the proportion of total cytoplasmic volume (V(v)) contributed by the CLIC pathway. We used both Cav1$^{-/-}$ and WT MEFs to compare cells with and without caveolae, as well as a fibroblast cell line, NIH3T3 (Fig. 2 A). In untreated Cav1$^{-/-}$ MEFs, total CTxB-labeled structures occupied 0.10 ± 0.01% of the total cytoplasmic volume after 15 s of internalization, 0.19 ± 0.01% after 1 min, and 0.50 ± 0.04% after 2 min (Fig. 2 B, Untreated). WT MEFs internalized similar volumes as Cav1$^{-/-}$ MEFs, indicating that caveolae contributed an insignificant proportion of internalization at this time. Intriguingly, when treated with Dyngo4a, under conditions where uptake of Tf is completely blocked and CLICs remain the only detectably active pathway, internalized CTxB-HRP still accounted for 0.09 ± 0.01% of cytoplasmic volume after 15 s, 0.16 ± 0.02% after 1 min, and 0.37 ± 0.02% after 2 min (Fig. 2 B, Dyngo4a). This indicates that 90.0% of the total endocytic volume is contributed by the CLIC pathway after 15 s of uptake, 85.9% after 1 min, and 74.0% after 2 min.

Confirmation of such high contribution of CLICs to total internalization was provided using strict ultrastructural criteria to compare the volume of tubular/ring-shaped structures (CLICs) and coated/vesicular structures (CCVs) in NIH3T3 cells that were not treated with any inhibitor (Fig. 2 C). Note that previous studies have shown that at the earliest times used here, Tf-HRP only labels CCVs as defined morphologically (Kirkham et al., 2005) but CTxB-HRP labels CCVs, caveolae, and CLICs. NIH3T3 cells internalized similar volumes to primary MEFs, with total CTxB-labeled structures after 2 min accounting for 0.47 ± 0.014% of cytoplasmic volume and tubular/ring elements (CLICs) contributing 78.7% (0.37 ± 0.014%) of that volume (Fig. 2 C). This alternative method avoids the need for inhibition of the dynamin-dependent pathways and suggests that under these conditions CLICs are not a compensatory pathway induced after acute dynamin inhibition (Damke et al., 1995). To confirm the striking contribution of the CLIC pathway to cellular internalization, V(v) measurements were next collected using free HRP, which cannot bind to membranes and induce clustering of microdomains (Fig. 2 D). Again, CLICs, morphologically defined as tubules/rings, constituted ∼74% of all HRP internalization after 2 min (V(v) 0.32 ± 0.05%).

To further confirm these results using an alternative method for assessment of endocytic contribution, CTxB was biotinylated and internalized in Cav1$^{-/-}$ MEFs, in the presence or absence of Dyngo4a. Surface-accessible biotin was cleaved and the remaining, internalized biotin measured by Western blot using streptavidin-HRP. Using this alternative biochemcial method CTxB-biotin levels in Dyngo4a-treated cells were equivalent to 76.0 ± 8.4% of that in untreated control cells after 2 min of uptake (Fig. 2 E). Agreement between morphometric and biochemcial approaches (and with V(v) measurements using a specific marker of the CLIC pathway: see below) provides important confirmation of the validity of the methods used and the significant magnitude of the CLIC pathway.

We next estimated the contribution of this pathway to total plasma membrane surface endocytosis. By measuring the surface-to-volume ratio (S(v); see Materials and methods) of a typical CLIC (Fig. 2 F) and the absolute volume of an average Cav1$^{-/-}$ MEF (2,346.7 ± 289.3 μm^3; see Materials and methods), the compiled membrane surface area of CLICs was calculated after 15 s of internalization to be 97.1 ± 10.9 μm^2. Given that the estimated average PM surface area of a Cav1$^{-/-}$ MEF was found to be 4,375.7 μm^2 (see Materials and methods), the equivalent of the total PM surface area could internalize through CLICs in less than 12 min (or 17 min after most extreme correction factor; see Materials and methods). Together these data indicate that CLICs provide a substantial capacity of internalization, more than any other constituite endocytic pathway in fibroblast cells.

CLICs exhibit the properties of a complex sorting compartment

Aside from the 2D morphological description of tubular CLICs, there is currently no data describing the 3D attributes of the primary carriers. To comprehensively visualize the ultrastructural properties of CLICs, high resolution electron tomography was performed on CTxB-HRP–laden structures (Fig. 3 A; Video 1). As a membrane marker, CTxB-HRP provided superior delineation of membrane profiles compared with free HRP at the concentrations and very early time points used here. CTxB-HRP was internalized for only 15 s to capture the earliest morphology of the carriers. The DAB reaction was performed on live cells to stabilize the morphology of the structures before glutaraldehyde fixation, simultaneously providing the necessary contrast for high resolution tomography and maintaining a close-to-native morphology. Morphology of DAB-labeled structures was similar in cells fixed before DAB reaction (not depicted). Images of 3D rendering from electron densities are shown (Fig. 3 A). There is clear evidence of vesicular membrane invaginations (Fig. 3 A, arrows), excluded from CTxB-HRP labeling, indicating that CLICs may have a capacity to bud internal membranes. Additionally, the tubular structure forms a complete ring, a facet previously overlooked (Fig. 3 A, arrowhead). As chemical fixatives can alter the morphology of endosomes (Murk et al., 2003), it was also important to confirm these observations without the use of aldehyde fixation. Therefore, CTxB-HRP was internalized for 15 s, DAB reaction performed, and the samples were high pressure frozen (HPF) as described previously (Richter et al., 2008). HPF CTxB-HRP–laden CLICs showed identical features to chemically fixed samples (Fig. 3 B), with vesicular invaginations from the limiting membrane and tubular ring-shaped extensions. Rather than simple tubules or vesicles, these primary carriers have a surprising degree of complexity.

Identification of novel CLIC-associated proteins

To identify CLIC associated components, we next sought to enrich CLICs away from other cellular material by density gradient fractionation (see Materials and methods). To increase the number of CLICs within a population of cells, the PI_3K inhibitor wortmannin was used within a previously developed system

Published August 16, 2010

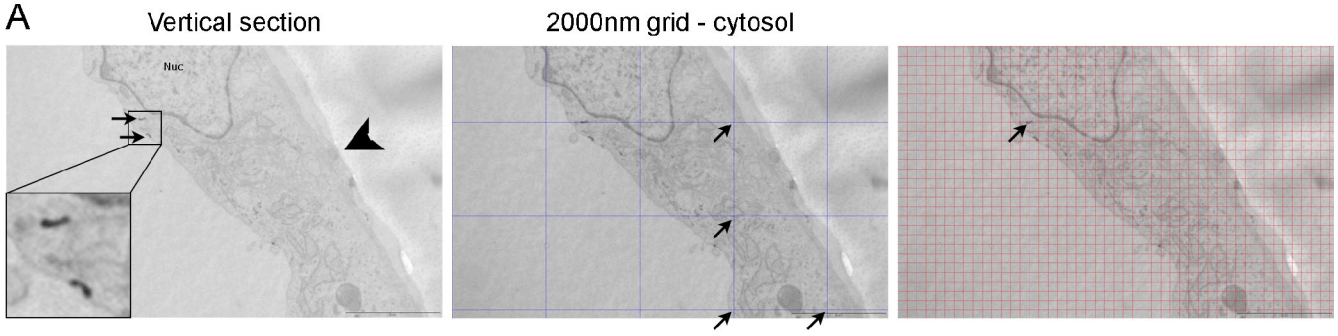

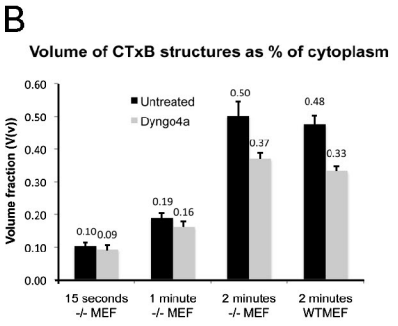

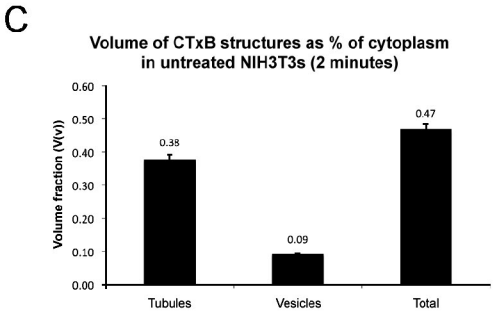

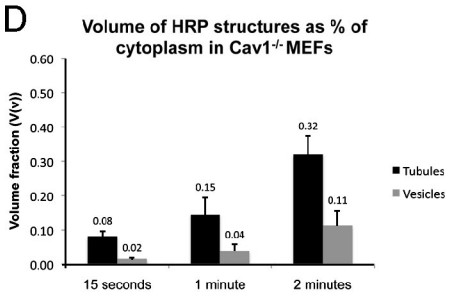

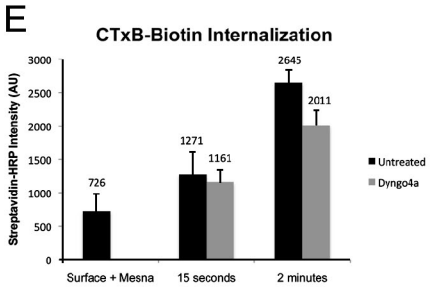

F

Time of internalization	V(v)	Absolute Volume (μm³)	S(v)	Absolute Surface Area (μm²)*	Volume per CLIC (μm³)+	CLICs per time
15 seconds	0.09 (0.06)	2.18 (1.41)	44.44	97.1 (63.1)	0.0026	831 (540)
1 minute	0.16	3.80				
2 minutes	0.37	8.70				

* based on average total cytoplasmic volume of 2346.7 μm³
+ calculated from volume of CTxB contained within whole-mount profile of CLIC
Estimates after correction in brackets

Figure 2. **Quantitation of CLIC endocytosis.** (A) Cav1$^{-/-}$ or wild-type (WT) MEFs were left untreated or were treated with Dyngo4a. CTxB-HRP was internalized for 15 s, 1 min, or 2 min. Examples of CTxB-labeled structures after 15 s of uptake are shown (inset, left panel). Substratum indicated by large arrowhead, grid sizes are 2,000 or 200 nm, examples of intersections shown by arrows. (B) 20–25 cells treated as in A were used to calculate the volume fraction (V(v)). Error bars show SEM. (C) NIH3T3 cells not treated with inhibitor were processed as in A and counted as in B. V(v) was calculated for both tubular and vesicular structures. Error bars show SEM. (D) Cav1$^{-/-}$ MEFs were incubated with HRP for 15 s, 1 min or 2 min and HRP-laden carriers counted as in B. Error bars show SEM. (E) CTxB was conjugated with NHS-SS-biotin and added to untreated Cav1$^{-/-}$ MEFs or Cav1$^{-/-}$ MEFs treated with Dyngo4a for 15 s or 2 min or was bound to untreated cells on ice for 10 min (Surface + MesNa). Cells were placed on ice and residual surface biotin cleaved with MesNa. Western blots of cell lysates were probed with streptavidin-HRP. Chart represents the average intensity of streptavidin-HRP across three independent experiments. Residue luminescence in Surface + MesNa samples indicates level of uncleavable biotin. Error bars show SEM. (F) Absolute volume of CLICs was estimated from the volume fraction, V(v), multiplied by the average volume of a Cav1$^{-/-}$ MEF, 2,347 μm^2. Surface density (S(v)) was calculated from high resolution images of labeled structures using a cycloid grid as described in Materials and methods and multiplied by the absolute volume to give absolute surface area. Volume of a single carrier was calculated as described in Materials and methods. Number of CLIC budding events per minute per cell was calculated based on the absolute volume internalized by all CLICs divided by the volume of a single carrier. Volume adjustments for overprojection effects are in brackets (see Materials and methods).

Published August 16, 2010

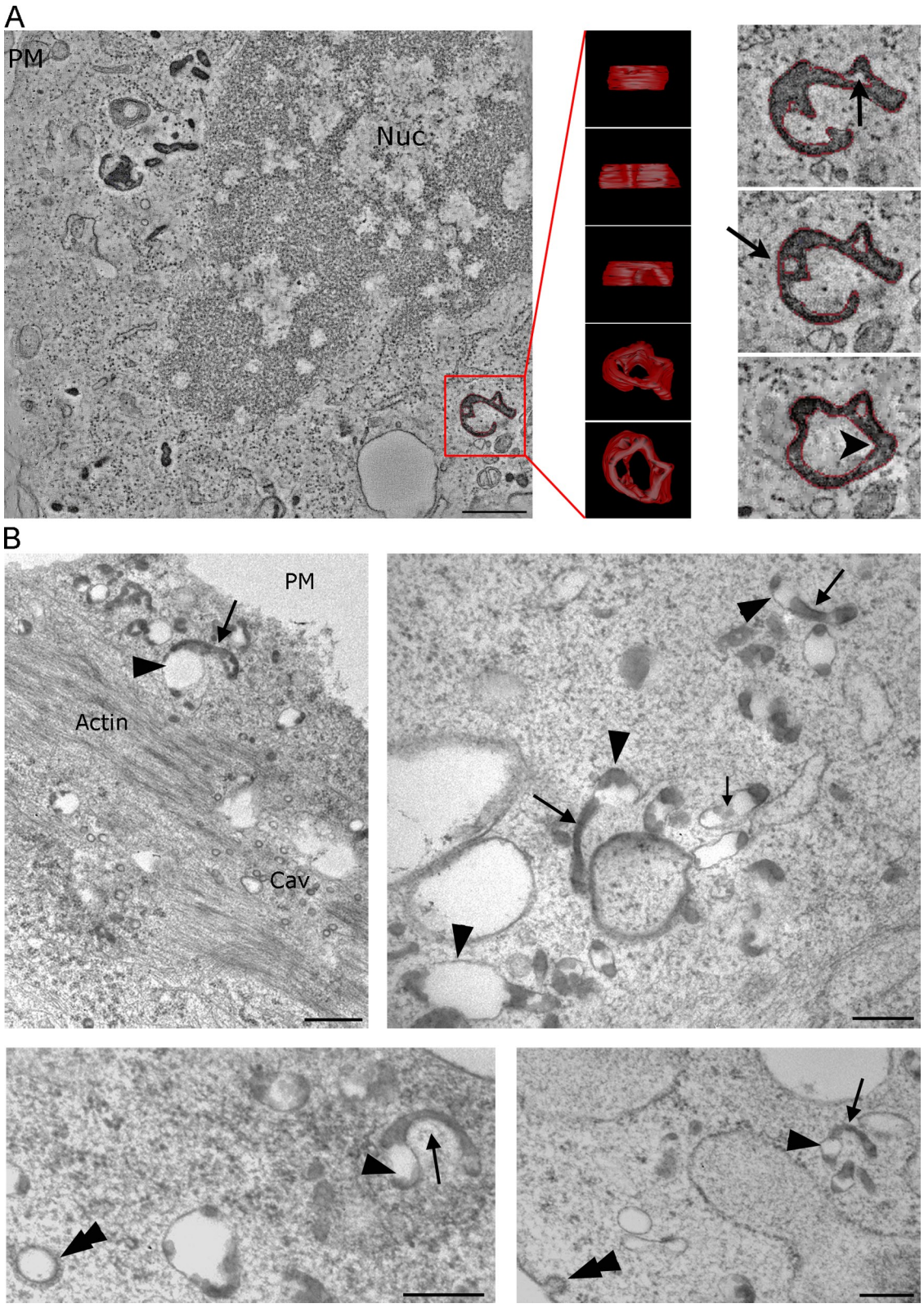

Figure 3. **3D morphology of CLICs.** (A) Cav1$^{-/-}$ MEFs were incubated with CTxB-HRP for 20 min on ice, before internalization for 15 s. The DAB reaction was performed and cells were processed for electron tomography (see Materials and methods). A single section of the original tomogram is shown (left). Various rotations of a 3D contoured electron density render were generated (middle). Enlarged sections selected from the tomogram (right) show internal vesicles (arrows) and a complete connection around the circumference of the structure (arrowhead). (B) WT MEFs grown on sapphire discs were incubated with CTxB-HRP for 15 s before DAB reaction and high-pressure freezing. Tubular extensions (large arrows) are seen emanating from vesicular bulbs (arrowheads) in the characteristic ring-shaped CLIC morphology. CCPs without CTxB label (double arrowheads) indicate that they are still surface connected. Bars, 200 nm.

Published August 16, 2010

that inhibits the fusion of CLICs with EEs (Kalia et al., 2006; Fig. S1). Using anti-GFP in GFP-GPI–expressing NIH3T3 cells (3T3-GPIs) as a marker for CLICs, we optimized conditions to concentrate GFP-GPI–positive membranes (Fraction 1.2; Fig. 4 A). CCVs (identified by clathrin heavy chain; CHC), EEs and recycling endosomes (REs; identified by TfR), and Golgi (identified by GM130) were below the detection limits within this fraction. However, this fraction also contained Cav1 (caveolae) and Grp78 (ER). The 10% fraction (Fraction 1.2) was, therefore, subjected to a second, continuous Nycodenz gradient, which provided a reproducible enrichment of anti-GFP–positive membranes (Fraction 2.8; Fig. 4 A). To further characterize the enriched fraction, we examined the membranes in detail by whole-mount EM (Fig. 4 B). Consistent with CTxB-HRP–laden CLICs visualized by EM in intact cells (Kirkham et al., 2005), the predominant structures within Fraction 2.8 have the striking morphology of CLICs. A low magnification image shows the consistent morphology of the structures enriched within this fraction (Fig. S2 A). At high magnification (Fig. 4 C, arrows), the structures within Fraction 2.8 were also consistent with tomography and HPF data (Fig. 3). Other structures displayed a clear connection between tubular extensions and spherical bulbs (Fig. 4 C, arrowheads). There was no evidence of contamination by other cellular compartments, such as mitochondria. Other fractions were enriched in structures distinct from those found in Fraction 2.8 (Fig. S2 C). This system also gave optimal, but incomplete, separation of GFP-GPI–positive carriers from Cav1 and Grp78. To quantify the membrane enrichment in Fraction 2.8 we analyzed internalized CTxB-HRP within the fraction after 5 min of internalization (Fig. 4 D, arrows). CTxB-HRP–labeled structures constituted 70.0 ± 0.9% of the membranes in the CLIC-enriched fraction as calculated from stereology (Fig. S2 B).

The validity of this method was further examined by analyzing membranes within Fraction 2.8 after inhibition of CLIC endocytosis. Using two independent methods of CLIC perturbation, expression of a Cdc42 dominant-negative mutant (Cdc42-DN; Sabharanjak et al., 2002) and cholesterol depletion with methyl-β-cyclodextrin (mβCD) under conditions where CME is unaffected (Kirkham et al., 2005; Glebov et al., 2006), there was a substantial reduction of CTxB and anti-GFP–positive membranes within Fraction 2.8 (Fig. 4 E; 59.7% reduction in CTxB levels in cells transfected with Cdc42-DN compared with Cdc42-WT; 53.6% reduction in anti-GFP antibody levels after treatment with mβCD). Thus, this approach shows concentration of CLIC marker positive membranes within Fraction 2.8 and reduced accumulation of these membranes after treatments known to inhibit CLIC endocytosis.

Unlike CHC and TfR, there was a small proportion of dynamin specifically concentrated in Fraction 2.8 (Fig. 4 F). Although dynamin is not necessary for the formation of nascent CLICs (Sabharanjak et al., 2002; Kirkham et al., 2005), it has been previously noted that expression of the DynK44A mutant reduces CTxB trafficking to the Golgi (Le and Nabi, 2003; Kirkham et al., 2005), independently from clathrin (Torgersen et al., 2001), suggesting a role in clathrin-independent CTxB uptake. As CLICs rapidly mature, however, it is difficult to assess a possible transient recruitment of dynamin under steady-state conditions. Therefore, colocalization between dynamin and anti-GFP in GFP-GPI–expressing cells was assessed after treatment with wortmannin (Fig. S3). Colocalization after 10 min was significantly increased in wortmannin-treated cells compared with untreated controls (13.1 ± 1.1% untreated; 39.2 ± 2.0% 100 nM wortmannin; Fig. S3, A and B), indicating that dynamin is recruited to CLICs rather than localizing to them from the PM. By EM, dynamin was also found on a small proportion of CTxB-HRP containing tubular/ring-shaped structures (Fig. S3 C). Although the majority of dynamin coincides with the CHC profile, the small but specific concentration in Fraction 2.8, as well as colocalization with GFP-GPI and CTxB, is consistent with the hypothesis that dynamin is recruited to CLICs, after PM scission.

To verify that membranes in Fraction 2.8 represent bona fide CLICs, 3T3-GPI cells were transfected with one of two markers for the CLIC pathway, Flot1-HA and GRAF1-myc. By Western blot analysis both endogenous and transfected Flot1 and GRAF1 were concentrated in Fraction 2.8 (Fig. 4 F). When fractions from transfected cells were labeled with anti-HA or anti-myc antibodies, a significant proportion of the structures within Fraction 2.8 were labeled (Fig. 4 G, arrows; 31.5 ± 2.5% Flot-HA and 41.3 ± 6.4% Graf1-myc positive). Comparatively, when Fraction 2.8 was labeled for endogenous Cav1, very few of the structures were positive (5.5 ± 0.8%) and, notably, these smaller vesicular structures were distinct from the CLIC-like structures (Fig. 4 G, arrowheads). Endogenous dynamin labeled a significant population of structures within Fraction 2.8 (Fig. 4 G, arrows; Fig. S3 D), supporting the notion that dynamin can associate with CLICs. We next used this fractionation approach to identify novel CLIC components.

The protein complement of Fraction 2.8 was examined after separation using 5–15% SDS-PAGE and the entire lane was cut into 2-mm slices, digested with trypsin, and analyzed by liquid chromatography mass spectrometry (LC-MS/MS; see Materials and methods). This identified 80 proteins with two or more peptide hits of 99% confidence (key targets and links to endocytosis in Table I, full list in Table S1). A significant cluster of proteins identified play a role in cellular adhesion and interaction with the ECM. Thy-1, a glycosylphosphatidylinositol-anchored protein (GPI-AP), is a critical component of focal adhesion disassembly through FAK phosphorylation (Rege et al., 2006). This interaction is dependent on the GPI anchor of Thy-1, implicating the GPI-AP–enriched CLIC pathway as a mediator of FAK activation. Integrin-β_1 is also a key component of focal adhesions and galectin3 is directly involved in clathrin-independent integrin-β_1 endocytosis (Furtak et al., 2001). Although a role for CME during integrin-β_1 endocytosis and cellular motility has been established (Palamidessi et al., 2008), it has also been found that integrin-β_1 uptake can be independent from clathrin and is mediated by lipid rafts (Vassilieva et al., 2008). Rap1 transmits outside-in integrin signals, leading to cell polarization, and its activation at the leading edge is necessary for chemokine-induced cellular migration (Shimonaka et al., 2003). CD98 also mediates integrin signaling during cell spreading and is localized to cell–cell contacts (Feral et al., 2005), where it activates Rap1 (Suga et al., 2001). Activation of Rap1 also leads to recruitment of CD44 to the leading edge (Shimonaka et al., 2003),

Published August 16, 2010

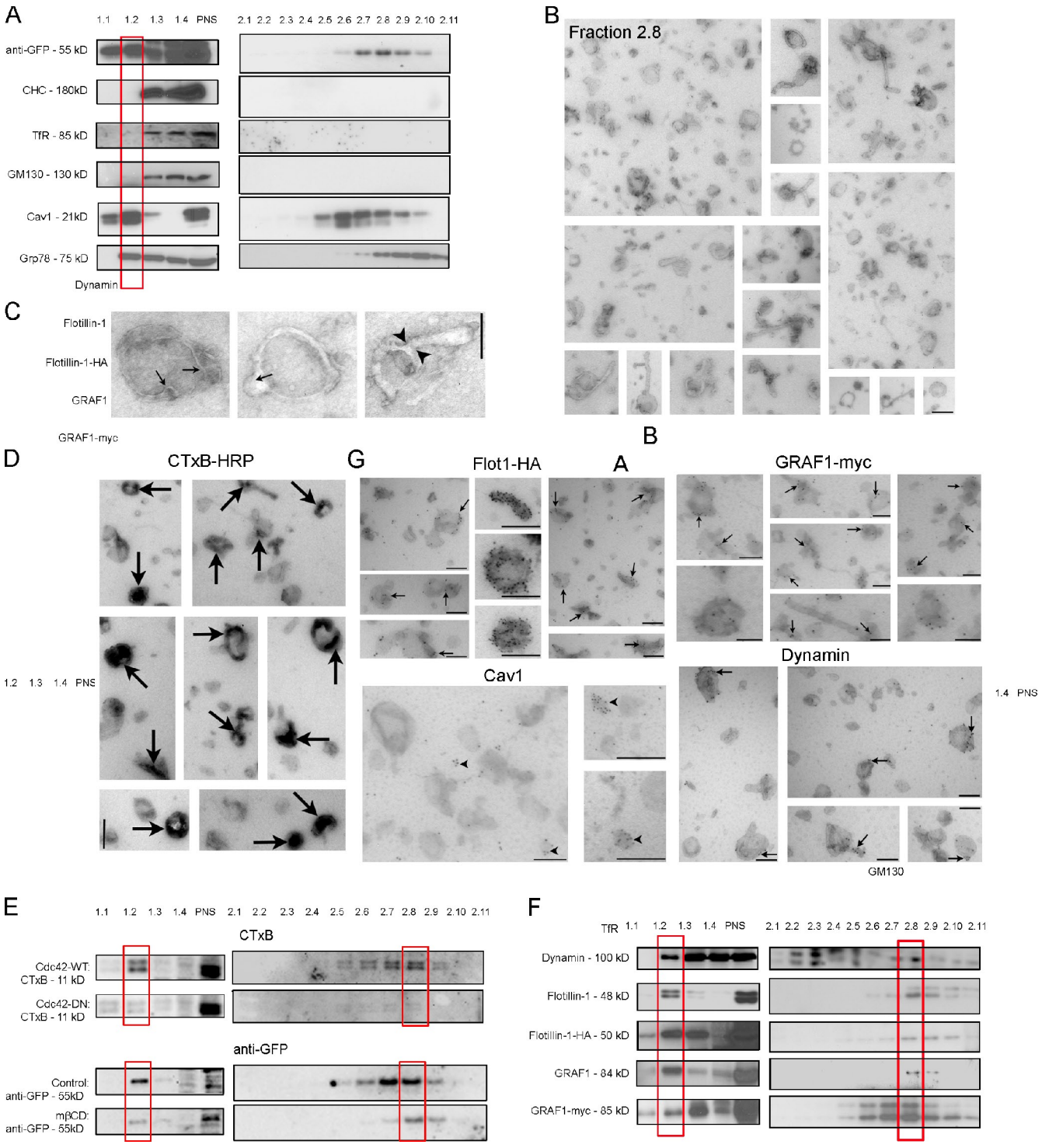

Figure 4. **Biochemical enrichment of CLICs.** (A) 3T3-GPI cells were subjected to density fractionation as described in Materials and methods. Western blots of membrane markers are shown. Within the first gradient (left) anti-GFP–, Cav1-, and Grp78-positive membranes are present in Fraction 1.2, highlighted by outline. CHC-, GM130-, and TfR-positive membranes are below the detection limit within this fraction. Within the second gradient, anti-GFP–positive membranes concentrate within Fraction 2.8, highlighted by outline. This represnts a yield of 9.6 ± 0.2% of anti-GFP–positive membranes. Cav1 concentrates in Fraction 2.6 and Grp78 in Fraction 2.10. (B) Fraction 2.8 was fixed and visualized by EM. Structures within Fraction 2.8 share similar profiles to CLICs seen within intact cells. Bar, 200 nm. (C) High resolution electron micrographs of Fraction 2.8 structures, providing examples of vesiculation (arrows) and a spherical bulb connected to tubular extension (arrowheads). Bar, 100 nm. (D) NIH3T3 cells were incubated with CTxB-HRP before fractionation and the DAB reaction was performed on Fraction 2.8. Bar, 200 nm. (E) NIH3T3 cells transfected with Cdc42-WT or -DN were incubated with CTxB before fractionation. Western blots were probed with anti-CTxB. 3T3-GPI cells were treated or not with mβCD before incubation with anti-GFP antibodies. Western blots of fractions were probed with anti–Rb-HRP. (F) Western blots of fractions from cells transfected with Flot1-HA, GRAF1-myc, or left untransfected. Fractions were probed with anti-HA, -myc, -dynamin, -Flotillin1, or -GRAF1 antibodies as appropriate. (G) Fixed sampled from F of Fraction 2.8 were labeled for anti-HA, anti-myc, endogenous Cav1, or dynamin. Structures labeled with Flotillin-1-HA, GRAF1-myc, and dynamin (arrows) or Cav-1 (arrowheads) are shown. Bars, 200 nm.

Published August 16, 2010

Table I. **Key targets identified from isolation of CLIC-positive fraction**

Target	Location	Link to endocytosis
4F2 cell surface antigen heavy chain/CD98	PM	Receptor for Galectin3 and Integrin β-1 endocytosis
78-kD glucose-regulated protein	PM/ER	Associates with lipid rafts and receptor for MHCI
Actin, cytoplasmic 1	Cytosol	Drives endocytic carrier formation
Alpha-2-HS-glycoprotein/Fetuin	PM/E	Endocytosis mediated by AnnexinA2
Annexin A2	E	Binds glycoproteins during endocytosis
CD109 antigen	PM	Cell surface GPI-AP
CD44 antigen	PM	Hyaluronan receptor
Collagen	ECM	ECM constituent
Fructose-bisphosphate aldolase A	Cytosol	Mediates Snx9-dynamin interaction
Galectin-3	PM	Mediates Integrin β-1 endocytosis
Guanine nucleotide-binding protein Gα(i,o)	PM	Involved in STAT3 signaling
Integrin β-1	PM	Receptor for ECM
Lysosome-associated membrane glycoprotein 2	E	Lysosomal membrane regulator
Membrane-associated progesterone receptor component 1	PM/ER	Involved in cholesterol homeostasis, rapidly cleared from the PM by endocytosis
Moesin	PM	Links CD44 to cortical actin to drive features in the PM
Myoferlin (Fer-1–like protein 3)	PM	Involved in Ca^{2+}-promoted membrane fusion; binds to AHNAK
Neuroblast differentiation-associated protein AHNAK	PM	Binds Myoferlin and Dysferlin and with Annexin2 mediates membrane fusion
Prolow-density lipoprotein receptor-related protein 1 (LRP1)	PM	Contains both tyrosine and di-leucine sorting motifs; binds saposin on cell surface
Prosaposin	PM/E	Co-receptor with LRP1; binds GM1
Rac1	PM/E	Induces membrane ruffling
Rab-11A	E	Endosome recycling
Rab-14	E	Endosome recycling
Rab-7a	E	Late endosome fusion and motility
Rab-5A	E	Early endosome fusion and motility
Rap-1b	PM	Integrin β-1 endocytosis and focal adhesion turnover; mediates STAT3
Receptor expression-enhancing protein 5	PM	Involved in Rab-mediated membrane trafficking
Reticulon-4	PM/ER	Tubulates membranes; binds NogoR, a GPI-AP at the PM
Thy-1 membrane glycoprotein	PM	GPI-AP; regulates FAK signaling
Tmp21	PM	Contains KDEL sequence, traffics to the PM independently from p24
Vimentin	Cytosol	With Annexin A2 regulates FAK signaling

E, Endosomes; ECM, extracellular matrix; ER, endoplasmic reticulum; PM, plasma membrane.

while CD44 is linked to integrin-β_1 signaling by forming specialized lipid raft microdomains (Lee et al., 2008). CD44 is also an important component of extracellular contact, involved in the degradation of ECM, and is involved in maintenance of polarization and directionally persistent migration (Mrass et al., 2008). This also implicates CLICs as a mediator of cell adhesion and, given the proposed ability for CLICs to recycle directly to the PM, presents a rapid recycling mechanism during cellular adhesion turnover and motility. Supporting this, moesin directs actin-based rearrangements of lipid rafts directly through CD44 to orchestrate the topology of cell surface structures, such as filopodia (Bretscher et al., 1997), and the CD44-ERM (ezrin-radixin-moesin) association is a critical component of directional cellular motility (Legg et al., 2002). We next sought to verify some key targets as novel cargo for the CLIC pathway.

Verification of novel CLIC proteins

Preliminary verification of some key targets was performed by comparison to internalized CTxB-555 and Tf-647 (Fig. 5 A). Anti–Thy-1, anti-CD44, and myoferlin colocalized with CTxB-555 but not Tf-647 in NIH3T3 cells after 2 min of uptake, indicating they are specific cargo for the CLIC pathway. Interestingly, although only a low level of colocalization was seen between anti-GFP and Rab11 after 10 min (17.07 ± 1.49%) in untreated 3T3-GPI cells (Fig. 5, B and C), after treatment with wortmannin there was a significant increase in their colocalization after 10 min (41.12 ± 2.79%; Fig. 5, B and C). As wortmannin inhibits the maturation of CLICs, this localization is not likely to occur within REs. Additionally, there was no detectable TfR in the CLIC-enriched fraction, arguing against significant contamination of RE membranes within this fraction.

Additional evidence for the sorting capability of CLICs was identified by assessment of the endocytic maturation of CD44. Endocytosis of CD44 was consistently Tf negative (Fig. 5 D), while it colocalized with CTxB after 2 min, with less overlap after 10 min. Persistent colocalization was also seen between CD44 and dysferlin from 2 to 40 min (Fig. 5 D). As dysferlin also remains distinct from the classical endocytic network

Published August 16, 2010

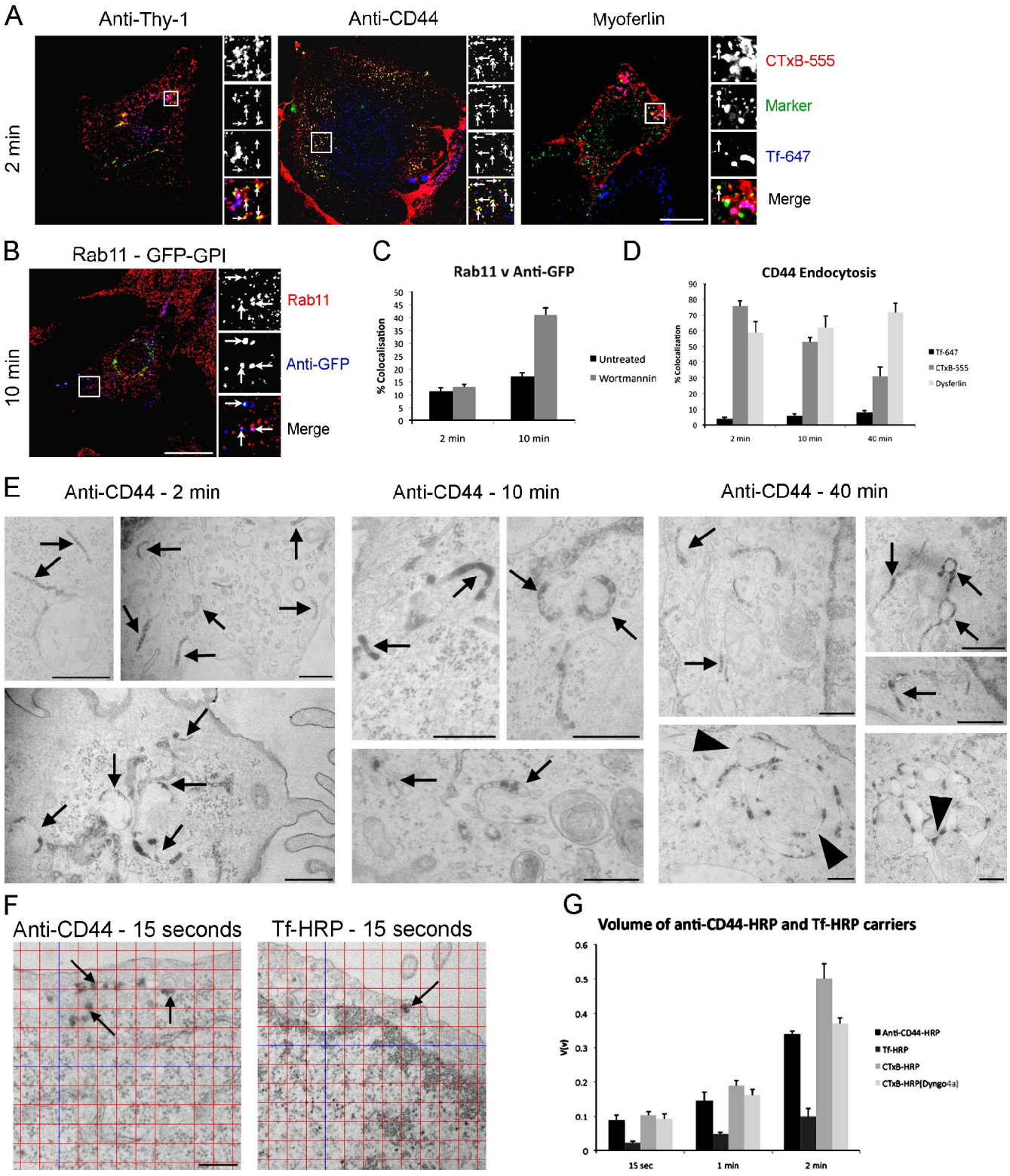

Figure 5. **Verification of novel CLIC cargo.** (A) NIH3T3 cells were incubated with either anti–Thy-1 or anti-CD44 antibodies and CTxB-555 and Tf-647 for 2 min. Myoferlin was detected after fixation, showing steady-state localization. Arrows indicate colocalization. Bar, 10 µm. (B) 3T3-GPI cells were left untreated or were treated with 100 nM wortmannin before internalization of anti-GFP for 10 min. Arrows indicate colocalization. Bar, 10 µm. (C) Quantitation of B from 12–15 cells in three independent experiments. (D) Quantitation of colocalization between internalized anti-CD44 antibodies and Tf-647, CTxB-555, or anti-myc antibodies for GFP-dysferlin-myc–expressing cells after 2, 10, and 40 min. Error bars show SEM. (E) Anti–CD44-HRP was internalized into WT MEFs before DAB reaction. Arrows show anti-CD44-HRP–positive carriers with morphology of CLICs. Arrowheads show large, tubular ring-shaped anti-CD44-HRP–positive compartment. Bars, 200 nm. (F) Anti–CD44-HRP or Tf-HRP was pulsed into Cav1$^{-/-}$ MEFs for 15 s, 1 min, or 2 min. Cells were fixed and processed for vertical sections. Arrows show HRP-labeled carriers. Bar, 200 nm. (G) Stereology measurements were captured across 20–25 cells in three independent areas as treated in F. Error bars show SEM.

Published August 16, 2010

(not depicted), this suggests that CLICs are directly sorting cargo rather than representing distinct populations of similar mechanisms. Confirming this, the ultrastructure of CD44-positive carriers, as visualized using anti–CD44-HRP, showed identical morphology to that of CTxB-HRP–laden CLICs (Fig. 5 E, arrows), whereas no label was found in the classical endosomal network. In some instances, intriguing tubular networks were seen with labeling for anti–CD44-HRP after 40 min of internalization (Fig. 5 E, arrowheads), possibly representing a mature compartment arisen from the CLIC pathway. The presence of anti-CD44 antibodies had no effect on the number or morphology of CTxB-HRP–laden CLICs between 2 and 40 min (not depicted), indicating that the CD44 antibodies do not influence the kinetics or ultrastructure of the pathway.

Using CD44 as a novel and specific marker for CLICs, it was also possible to confirm stereology calculations using CTxB-HRP in the presence of dynamin inhibition. Anti-CD44-HRP–conjugated antibodies or Tf-HRP was internalized in Cav1$^{-/-}$ MEFs and the DAB reaction was performed (Fig. 5, F and G). This method has the advantage of relying on the specificity of CD44 for the CLIC pathway and Tf-HRP for CME. We found that CD44-positive CLICs accounted for 0.09 ± 0.02% of the total cytoplasmic volume after 15 s, 0.14 ± 0.03% after 1 min, and 0.34 ± 0.01% after 2 min (Fig. 5 G). These volume estimates are in excellent agreement with those obtained using morphological criteria or using specific inhibitors of dynamin-dependent endocytosis (see above). These data identify a range of novel CLIC cargo, confirm the significant magnitude of the pathway, and provide evidence for the direct recruitment of dynamin and Rab11 to CLICs and the ability to sort cargo to distinct destinations.

Polarization of CLICs during cellular migration

Based on the association of novel CLIC cargo, such as Thy-1 and CD44 with extracellular attachment, we sought to visualize CLICs within migrating cells. As regulation of adhesion components is a fundamental process during cellular migration the CLIC pathway may be either up-regulated or spatially restricted within motile cells. A scratch-wound was applied to a confluent monolayer of fibroblasts and cells were allowed to migrate into the space provided by the wound. Early endocytosis of CTxB and Tf was assessed in the presence of either internalizing anti-CD44 or anti–Thy-1 antibodies or was followed by labeling for endogenous Cav1 (Fig. 6 A). Colocalization was seen between CTxB-555 and both CD44 and Thy-1 at the leading edge of migrating cells (arrows). In cells expressing GFP-GPI, anti-GFP antibody endocytosis also preferentially occurred at the leading edge (Fig. 6 A), indicating polarization of CLICs rather than polarized uptake of specific GPI-APs involved in migration, such as Thy-1. There was a clear spatial distinction between CTxB-555, Cav1, and Tf-647 in these cells, which was confirmed by assessing average pixel intensity across a selected field (Fig. 6 B). It has been well documented that Cav1 localizes to the trailing edge during 2D migration (Grande-García et al., 2007). We also found that CTxB binding after fixation was uniform over the entire cell, excluding the possibility that GM1 was polarized within these cells (not depicted).

To verify the polarization of CLIC endocytosis in migrating fibroblasts, ultrastructure of CTxB-HRP–laden carriers was assessed after a 2-min uptake in migrating MEFs (Fig. 5 C, large arrow indicates direction of migration). Labeled CLICs were predominantly found at the leading edge (Fig. 6 C; 1, 2). Conversely, an accumulation of unlabeled, surface-connected caveolae was seen at the trailing edge (Fig. 6 C; 3, 4 insets). Quantitation of the number of endocytic and surface-connected structures at the leading and trailing edges confirmed this polarized distribution (Fig. 6 D). Both surface-connected CCPs and internalized CCVs showed no preference for the leading or trailing edge. To our knowledge, this is the first evidence for a striking spatial distinction between the CLIC pathway, caveolae, and CME, and is suggestive of a role for CLICs during dynamic adhesion turnover specifically from the leading edge.

As the CLIC pathway is polarized during migration and internalizes key adhesion components at the leading edge, we speculated that this pathway could play a critical role during cell migration. Thus, a system was developed in which CLIC-dependent uptake could be inhibited without affecting CME (see Materials and methods). To optimize conditions for transient ablation of the CLIC pathway, we internalized CTxB-HRP for various short times, performed DAB-mediated ablation of the labeled compartments, and then analyzed the uptake of a subsequent pulse of CTxB-555, Tf-647, and antibodies to CD44. 2 min of CTxB-HRP internalization followed by the DAB reaction on living cells was found to give the strongest inhibition of CD44 and CTxB-555 endocytosis without any effect on Tf-647 uptake (Fig. 6 E). Under these conditions Tf-647 endocytosis and maturation was unaffected, even after a 40-min pulse, indicating the endosomal network was still functional (not depicted). The inhibition of CD44 and CTxB-555 internalization following CTxB-HRP–based ablation persisted for at least 4 h after the ablation step, indicating this assay could be used to assess possible effects of CLIC inhibition on migration. Quantitation of fluorescence intensity shows that CTxB-HRP inactivation of the CLIC pathway resulted in an 81.8 ± 7.2% reduction in CTxB-555 and a 93.8 ± 2.6% reduction in CD44 endocytosis, whereas Tf-647 internalization was not reduced (increased by 28.6 ± 24.8%) after a 4-h incubation (Fig. 6 F).

To test the requirement for CLIC endocytosis during migration, this inactivation assay was applied to migrating fibroblasts. The capacity of cell monolayers to migrate into a scratched wound was assessed by measuring the total distance between two cell fronts of a wound after CLIC inactivation. When CTxB-HRP was used to inactivate CLICs, without effect on other endocytic routes, cell monolayers had a reduced capacity to migrate into a wound after 4 h (15.8 ± 1.7% distance of wound closed; Fig. 6 G) compared with DAB only–treated cells (33.4 ± 3.7% closed). A similar effect was observed in Cav1$^{-/-}$ fibroblasts, ruling out the possibility that the migration defect was due to inactivation of caveolae. Together with previous studies (Grande-García et al., 2007; Nishimura and Kaibuchi, 2007), these findings suggest that three major endocytic routes in eukaryotic cells, CME, caveolae, and the CLIC pathway, are all important for normal directional cell migration.

Published August 16, 2010

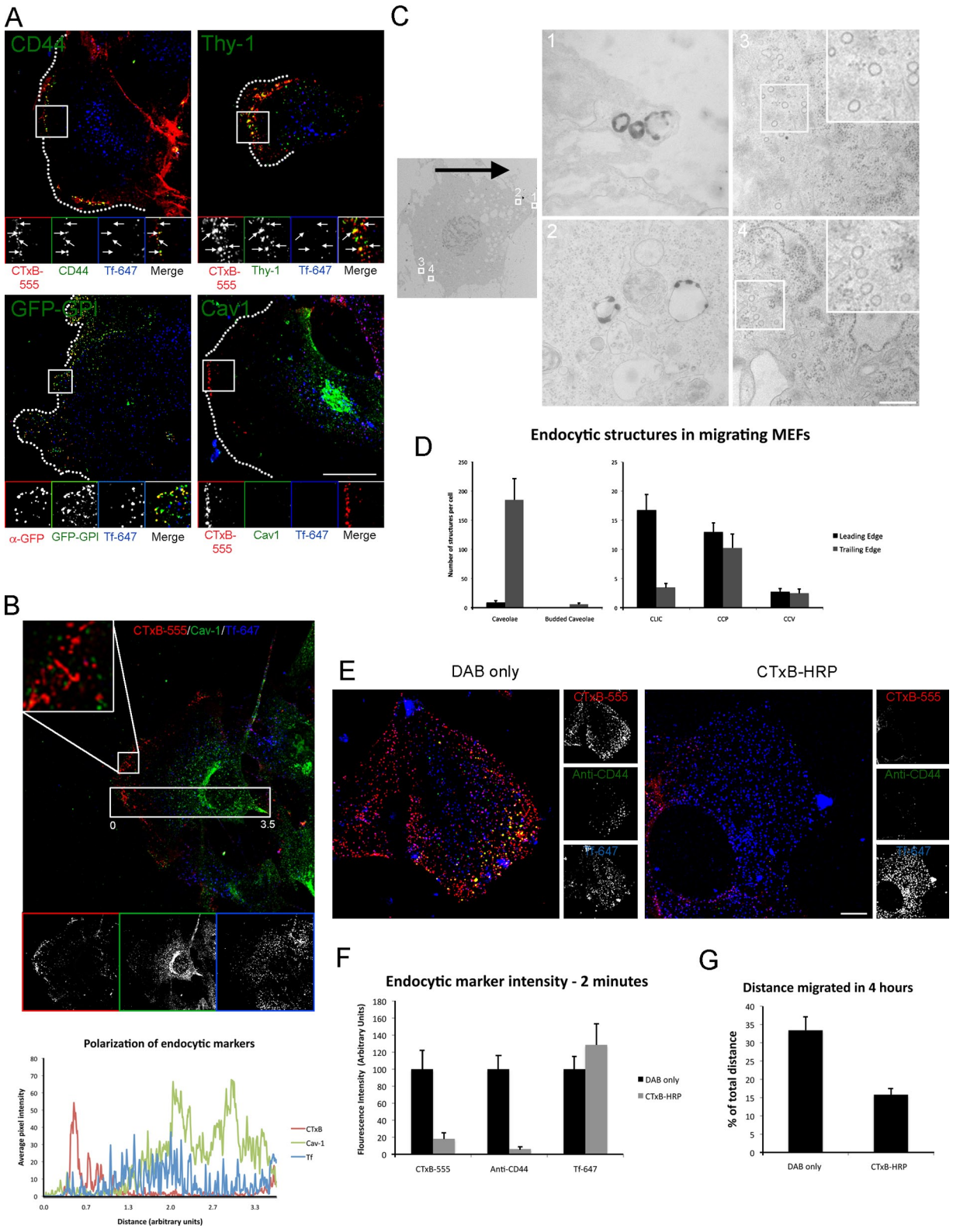

Figure 6. **CLICs become polarized during and are necessary for efficient cellular migration.** (A) Confluent monolayers of WT MEFs or NIH3T3s were scratched and cells were allowed to migrate for 8–12 h. CTxB-555 and Tf-647 were pulsed into migrating cells for 2 min in the presence of anti-CD44 (WT MEF), anti-GFP (GFP-GPI expressing WT MEF), or anti-Thy-1 (NIH3T3) antibodies or cells were labeled for Cav-1 (WT MEF). Dotted lines indicate leading edges. Arrows show colocalization between anti-CD44 or anti–Thy-1 and CTxB-555 but not Tf-647 at the leading edge. Bar, 20 µm. (B) Quantitation of average pixel intensity from the leading to trailing edges for CTxB-555, Cav-1, and Tf-647. Inset shows the concentration of tubular, Cav-1, and Tf-negative CTxB-labeled CLICs at the leading edge. A rectangular area, outlined, was used to calculate the average pixel intensity (along the y axis) across the leading to trailing edge (along the x axis) for each endocytic marker. Plot profiles identify a concentration of CTxB in the leading edge and Cav-1 in the trailing edge whereas Tf shows uniform intensity across the cell. Bar, 10 µm. (C) Electron micrographs of a migrating WT MEF. Large arrow indicates direction of migration. Magnifications from the leading edge and the trailing edge show representative images of CTxB-HRP–labeled CLICs

Published August 16, 2010

Discussion

Here we identify the CLIC pathway as a high capacity route that accounts for the vast bulk of constitutive fluid uptake in fibroblasts, implicating CLICs as key mediators of PM remodeling. Previous estimations of endosomal tubule volume using stereology have noted that tubules close to section thickness (55 nm) can lead to overprojection effects (Griffiths et al., 1989). When correction factors are applied to volume estimates CLICs would still account for over 70% of internalization. Bulk phase early endocytosis in rat fetal fibroblasts has also been shown to be independent from clathrin and occurs via a constitutive, noncaveolar pathway, which rapidly regurgitates substantial amounts of endocytic volume (Cupers et al., 1994). We have previously shown that up to 40% of endocytosed fluid, mainly internalized through the CLIC/GEEC pathway, is regurgitated in 5 min (Chadda et al., 2007). Together, this suggests that the CLIC pathway internalizes and returns significant portions of the PM quickly, rapidly turning over membrane during key cellular processes, such as PM repair and homeostasis. It also provides the endocytic system with a mechanism to remodel features of the PM quickly, critical for extracellular interactions during various processes ranging from adhesion to signaling. Such vast membrane flow and recycling has recently been observed from a GPI-AP–positive CIE compartment, which provides a signficant fraction of the required membrane during cellular spreading (Gauthier et al., 2009).

Calculation of fluid uptake via clathrin-independent endocytosis has generally estimated the contribution of these routes to be 40–60% of total fluid internalization (Sandvig et al., 1987; Sabharanjak et al., 2002; Cheng et al., 2006). The higher contribution of 74%, calculated here, may be explained through differences in the resolution, both spatial and temporal, of experimental procedures used. By calculating volume internalized based on ultrastructure rather than fluorescence this work provides a higher resolution analysis than previous studies, which were limited by the optical resolution of fluorescence microscopy.

The 3D structure of CLICs identifies them as pleiomorphic, complex, multicomponent carriers. Although it is recognized that the bulk of CLIC-internalized fluid and membrane fuses with EEs, discrepancies between the ability of CLIC cargos, such as dysferlin/myoferlin and CD44 compared with GFP-GPI and CTxB, to fuse with Tf-positive endosomes strengthens the argument that some domain of CLICs traffics distinctly from the bulk (Fig. 7 A). Recruitment of dynamin to CLICs, after budding from the PM, further demonstrates the sorting complexity of the route. Although dynamin is not necessary for scission of CLICs from the PM (Kirkham et al., 2005; Sabharanjak et al., 2002), such recruitment of dynamin to maturing CLICs, after the initial scission, provides important machinery for CLICs to compartmentalize. Clearly, however, dynamin is not required for the generation of CLIC architecture, as the morphology of CLICs is identical in the presence or absence of dynamin inhibition. Recruitment of dynamin to CLICs as they mature would reconcile the direct interaction between GRAF1 and dynamin within this dynamin-independent pathway (Hansen and Nichols, 2009).

Myoferlin, a novel CLIC-associated target identified here, is a member of the ferlin family of proteins implicated in membrane fusion (Davis et al., 2000). We have previously shown that another ferlin family member, dysferlin, associates with the CLIC pathway (Hernández-Deviez et al., 2008). Myoferlin, like dysferlin, is involved in calcium-dependent membrane fusion after mechanical disruption to the PM (Bernatchez et al., 2007). Recently, a clathrin-independent, GPI-enriched endocytic compartment has been implicated in membrane repair after PM shearing (Idone et al., 2008a,b). This raises the exciting possibility of links between the role of dysferlin/myoferlin in this process and the ability of CLICs to provide the necessary membrane for repair of PM lesions. Supporting this, two targets identified here, AHNAK and Annexin A2, have been shown to bind dysferlin and myoferlin during membrane repair (Huang et al., 2007). Localization of dysferlin/myoferlin to a subdomain of CLICs that does not merge with Tf-positive EEs highlights that this pathway has the capability to rapidly recycle membrane back to the PM under specific conditions, such as PM repair (Fig. 7 B).

Evidence for an association between CLICs and cellular migration is provided by the distinct polarization of CLICs in motile cells, as well as the impairment of migration after transient ablation of the pathway. Specific internalization of Thy-1 and CD44 through the CLIC pathway at the leading edge provides an explicit role for CLICs in rapid turnover of adhesion receptors within a spatially restricted mechanism. How CLICs become polarized during migration remains an open question; however, one possibility arises from activity of the initial regulator of the CLIC/GEEC pathway, Cdc42. Cdc42 was originally described as directing cell polarity during yeast budding (Johnson and Pringle, 1990) and plays an assortment of fundamental roles during eukaryotic cell polarization (Etienne-Manneville, 2004). After wounding of cell monolayers Cdc42 activity is specifically directed to the front of the cell, resultant from signaling between contacts and the ECM (Etienne-Manneville and Hall, 2001). As Cdc42 activity is necessary for formation of CLICs, this would lead to specific localization of CLICs at the leading edge of wounded monolayers. The clathrin adaptor, Numb, is also

(1, 2) and surface-connected caveolae (3, 4). Bar, 500 nm. (D) Quantitation of the number of endocytic structures at the leading and trailing edge of cells treated as in C. Budded caveolae and CCVs are positive for CTxB-HRP label, whereas caveolae and CCPs are not. Error bars show SEM. (E) WT MEFs were incubated with or without CTxB-HRP for 2 min. The DAB reaction was performed on live cells for 5 min. Cells were washed and allowed to grow for a further 4 h. CTxB-555, anti-CD44 antibodies, and Tf-647 were added directly to cells for 2 min of uptake before acid stripping and fixation. Bar, 10 µm. (F) 12–15 cells treated as in E were quantitated for average fluorescence intensity of CTxB-555, Tf-647, or goat anti–mouse-488 for mouse–anti-CD44. (G) Confluent monolayers of WT MEFs were scratched and cells were allowed to migrate into the space for 1 h. Cells were incubated with serum alone or serum with 10 µg ml^{-1} CTxB-HRP for 2 min and the DAB reaction was performed as in E. After 4 h of migration, cells were fixed and distance migrated was determined by measuring the distance of the gap between both sides of the wound at time zero and after 4 h of incubation. Error bars show SEM from three independent experiments.

Published August 16, 2010

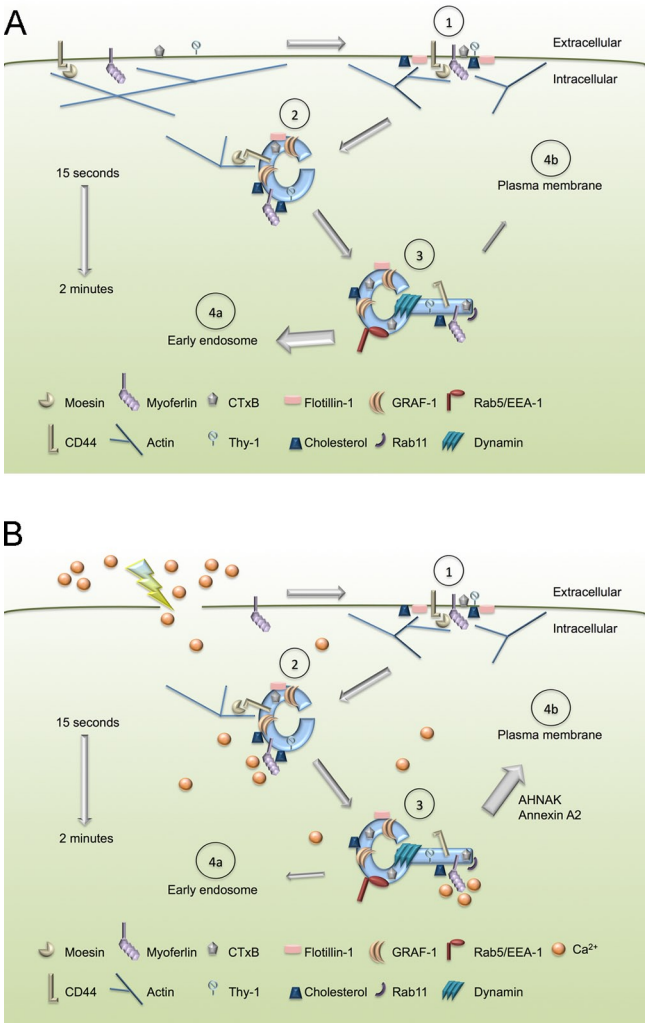

Figure 7. **Model of CLIC endocytosis.** (A) (1) CLIC cargo, such as Thy-1, CD44, and myoferlin are concentrated within Flotillin-1 and cholesterol-enriched microdomains. (2) Actin and GRAF-1 drive the initial formation of the carriers, within 15 s. (3) Recruitment of dynamin, Rab11, and Rab5/EEA-1 complexes within 2 min provides the ability for these carriers to facilitate bulk membrane flow to early endosomes (4a) and fast plasma membrane recycling (4b). (B) After abrasion to the PM an influx of Ca^{2+} activates the fusogenic C2 domains of dysferlin/myoferlin, resulting in the preferential recycling of the CLIC pathway.

specifically localized to the leading edge where it mediates integrin-β_1 endocytosis (Nishimura and Kaibuchi, 2007). It appears surprising that Numb-positive CCVs and CLICs both polarize to the leading edge during migration. One possible explanation for this is the types of cargo internalizing through each pathway. Adhesion components without a CCP sorting motif, such as CD44 and Thy-1, still need to be internalized for efficient migration and this could occur via CLICs at the leading edge. Consistent with such a hypothesis, a screen for genes involved in epithelial cell migration identified that knock-down of GRAF1, a regulator of the CLIC pathway (Lundmark et al., 2008), reduced the capacity of these cells to migrate (Simpson et al., 2008).

This study has shown the significant magnitude of traffic through this largely uncharacterized sorting compartment. Rather than acting as passive carriers that shuttle from the PM to EEs, we propose that CLICs arise from the plasma membrane and rapidly mature into a high capacity sorting station. We have shown that CLICs are a high capacity, dynamic, and complex sorting system and propose that they have the ability to sort subcompartments to distinct destinations for critical cellular processes such as membrane repair, migration, and maintenance of the PM.

Materials and methods

Internalization assay

Cells on 12-mm coverslips or 35-mm dishes were serum starved for 4 h in serum-free DME (Invitrogen) before two times 2-min wash in precooled CO_2-independent media (Invitrogen) on ice and placed on 50-µl drops of 10 µg.ml^{-1} CTxB-555 (Invitrogen), 5 µg.ml^{-1} Tf-488 (Invitrogen), and/or anti-GFP as desired for 20 min. For stereology, 35-mm dishes were not incubated on ice but were subjected to constitutive uptake at 37°C, 5% CO_2 for desired times. Coverslips were moved to prewarmed serum-free DME and incubated at 37°C, 5% CO_2 for desired times. Coverslips were placed back on ice in precooled CO_2-independent media. Two times 30-s 0.5 M glycine (pH 2.2) acid stripping was routinely performed before fixation in 2% paraformaldehyde. For immunocytochemistry, cells were permeabilized in freshly made 0.1% saponin for 10 min and blocked in 0.2% fish skin gelatin/0.2% BSA in PBS. Coverslips were incubated with primary antibodies for 1 h at room temperature, followed by three times 10-min wash in PBS before incubation with secondary Alexa Fluor–conjugated antibodies at 1:400 for 1 h.

Fluorescence micrographs were captured on a confocal laser-scanning microscope (Axiovert 200 m SP LSM 510 META; Carl Zeiss, Inc.). Images were captured under oil with a 63x Plan-Apochromat objective, at excitation wavelengths of 488, 543, and 633 nm for GFP-tagged constructs or Alexa Fluor 488–, Alexa Fluor 555–, or Alexa Fluor 647/660–conjugated antibodies, respectively. Band-pass and meta filters were applied as appropriate for respective fluorophores and images were captured from photomultiplier tube detectors (Carl Zeiss, Inc.). Colocalization was quantitated using Volocity v3.7. Images of individual cells were split into RGB channels, automatic thresholding applied, and colocalization coefficients calculated on percentage of overlapping voxels. Antibodies used include Thy-1 and CD44 (Abcam); CHC, GM130, Grp78, Cav1, and HA (BD); myc (Sigma-Aldrich); and TfR (Invitrogen). HRP-conjugated anti-CD44 was generated with Lightning-Link HRP conjugation kit (Innova Bioscience) as per the manufacturer's instructions.

Dynamin and PI3K inhibition

Cells were serum starved for 4 h in serum-free DME before incubation for 20 min with 30 µM Dyngo4a, 80 µM dynasore (Sigma-Aldrich), or 100 nM wortmannin (Roche). Cells were then incubated with an endocytic marker of interest in the presence of Dyngo4a and wortmannin for indicated periods at 37°C.

Electron microscopy and DAB reaction

After constitutive internalization of 10 µg.ml^{-1} CTxB-HRP (Invitrogen) at 37°C, cells were placed on ice and washed two times for 1 min in ice cold PBS, followed by 10 min in 1 mg.ml^{-1} DAB (Sigma-Aldrich) ± 50 µM ascorbic acid (AA) in PBS. Cells were then incubated with DAB ± 50 µM AA with 0.012% H_2O_2 for 20 min, followed by fixation in 2.5% glutaraldehyde (ProSciTech) in PBS for 1 h at room temperature. For plastic sections, cells were contrasted with 1% osmium tetroxide and 4% uranyl acetate. Cells were dehydrated in successive washes of 70%, 90% and 100% ethanol before embedding in LX-112 resin. For frozen sections, cells were scraped and embedded in 10% gelatin and gelatin blocks were infused with 2.3 M sucrose. Blocks were frozen onto mounting pins and 55-nm sections were collected using a UC6 ultramicrotome (Leica). Tomograms of 300-nm plastic sections were captured in 1° increments, tilted ±60° on a transmission electron microscope (model F30; Tecnai) using UltraScan 4000 semi-automated software. High pressure frozen samples were essentially processed as described previously (Richter et al., 2008). In brief, CTxB-HRP was added directly to cells grown on sapphire discs and DAB reaction was performed on ice before discs were frozen in a Balzers HPM010 high pressure freezer (BAL-TEC AG) and stored under liquid nitrogen. Freeze substitution was performed in acetone with 0.7% uranyl acetate; 1% osmium tetroxide at −90°C before warming to 0°C over 3 d and infiltrated with Embed 812-Araldite resin.

Published August 16, 2010

Nycodenz density fractionation

NIH3T3–GFP-GPI cells were serum starved and treated for 20 min with 100 nM wortmannin and 30 µM Dyngo4a. Anti-GFP antibodies were directly added to treated cells in the presence of wortmannin and Dyngo4a for 5 min at 37°C. Cells were placed on ice and harvested by scraping in TES buffer (10 mM tricine, 1 mM EDTA, and 250 mM sucrose, pH 7.4) with dissolved complete protease inhibitor cocktail (Roche). Cells were homogenized by passaging 10 times each through 21- and 27-gauge needles. A 17,000-*g* spin at 4°C for 10 min was applied to sediment nonlysed cells and nuclei. Post-nuclear supernatants were mixed with an equal volume 70% Nycodenz in TES and placed on the bottom of a four-step gradient, consisting of 25%, 10%, and 0% Nycodenz steps. Gradients were spun at 160,000 *g* for 2 h. The 10% fraction (excluding the interface) was collected and diluted 1/3 in TES with protease inhibitors and placed on top of a 5–20% continuous Nycodenz gradient. This was spun at 206,000 *g* for 2 h. Fractions were collected from the top of the gradient and TCA-precipitable samples analyzed by SDS-PAGE and LC/MS-MS. For visualization of Nycodenz fraction morphology by EM, 10 µl of fraction of interest was mixed with 10 µl 5% glutaraldehyde and a 100 mesh copper EM grid was placed on top for 30 min at room temperature. Grids were washed three times 5 min with PBS, followed by five times 2 min H_2O before staining with 1:9 (by volume) of 4% uranyl acetate to 2% methyl cellulose for 10 min on ice.

CTxB biotinylation

CTxB-555 was biotinylated with 2 $mg.ml^{-1}$ EZ-link Sulfo-NHS-SS-biotin (Thermo Fisher Scientific) for 10 min at 37°C and biotin quenched with 1:1 volume of 200 mM glycine for 5 min. CTxB-biotin was added to Cav1$^{-/-}$ MEFs either treated with 30 µM Dyngo4a or left untreated for the times indicated. After CTxB-biotin internalization, cells were placed on ice and stripped with three times 5-min washes with 100 mM MesNa (Sigma-Aldrich). MesNa was quenched with three times 5-min washes with 54 mM iodoacetamide (Sigma-Aldrich). Cells were harvested in TNE (20 mM Tris pH 7.5, 150 mM NaCl, and 5 mM EDTA) with complete protease inhibitors (Roche) and solubilized with 1% Triton X-100. BCA protein assays (Thermo Fisher Scientific) were routinely performed to accommodate equivalent loading. Western blots were probed with streptavidin-HRP (Invitrogen) in 5% skim milk, 0.1% Tween 20. Intensity of developed HRP chemiluminescent bands was determined for multiple exposures per sample in ImageJ using Gel Analyzer.

Stereology

Serum-starved cells were incubated directly with 10 $\mu g.ml^{-1}$ CTxB-HRP, 20 $mg.ml^{-1}$ HRP (Sigma-Aldrich), 10 $\mu g.ml^{-1}$ anti-CD44-HRP antibodies or 20 $\mu g.ml^{-1}$ Tf-HRP (Invitrogen) for desired times before being placed on ice, washed with precooled CO_2-independent media, and processed for the DAB reaction and EPON embedding. Vertical sections, visualized at 20,000x on a transmission electron microscope (model 1011; JEOL), were overlayed with a 2,000-nm square lattice grid using iTEM software. The number of intersections that fell on top of the cytoplasm, excluding the nucleus, were recorded across 20–25 cells and three independent areas. A 200-nm square lattice grid was also applied and intersections that fell on top of DAB-labeled structures were recorded as above. Number of points lying over DAB-labeled structures multiplied by the grid size was compared, as a percentage, to points over cytoplasm by grid size to give the percentage of labeled structures to cytoplasmic volume (V(v)). Overprojection effects on endosomal tubules can lead to volume overestimation as described previously (Griffiths et al., 1989). Based on the section thickness, average diameter, and length of CLICs, a correction factor of 0.65 can be applied to the V(v) measurements, based on graphs previously developed (Weibel, 1979). Correction factors are approximate only and give an estimate of possible error. Based on tomography data (Fig. 3), however, CLICs display a depth greater than section thickness (entire volume is still within 300-nm section, far thicker than 55-nm sections used for volume calculation), in which case overprojection effects become negligible.

Surface density, or surface volume fraction (S(v)), was calculated by placing a cycloid grid over high resolution images of CTxB-HRP–labeled structures and using the formula: $S(v) = 2I/P \bullet l(p)$, where I = total intersections of cycloid grid with structure of interest, P = total points of cycloid grid lying over structure of interest, and l(p) = length of the cyloid in µm, which was an absolute distance of 75 nm in this study.

Total cellular volume of a Cav1$^{-/-}$ MEF was calculated by binding CTxB-555 to fixed cells. Confocal Z-stacks were obtained from five representative cells and total average cellular volume was calculated using Volocity v3.7. Surface area of Cav1$^{-/-}$ MEF was calculated by finding the S(v) of plasma membrane across 25 cells, from low magnification electron micrographs, multiplied by the total average volume.

To capture the average volume of single CTxB-HRP–positive CLIC, high resolution electron micrographs from whole-mount profiles were used. As CTxB-HRP label (as well as HRP and anti-CD44-HRP label) was only found within the tubular ring of CLICs, we assumed that the entire volume of CLICs is comprised solely within the tubule space. Therefore, the volume of a sphere based on the diameter of the inner membrane was subtracted from the volume of a sphere based on the diameter of the outer membrane of the rings. This calculated that an average CLIC had an estimated volume of 0.00263 ± 0.00048 μm^3. In comparison, the volume of a single CCV was estimated to be five times smaller (0.0005 μm^3 assuming sphere based on diameter of 100 nm).

Mass spectrometry

An Agilent 1100 Binary HPLC system (Agilent Technologies) was used to perform reversed phase separation of the in-gel digests using a Vydac MS C18 300A column (150 mm × 2 mm) with a particle size of 5 µm (Vydac). Mass spectrometry experiments were performed on a hybrid quadrupole/linear ion trap 4000 QTRAP MS/MS system (Applied Biosystems). All analyses were performed using information-dependent acquisition and the linear ion trap (LIT) acquisition modes. Analyst 1.4.1 software was used for data analysis.

Cell migration

Confluent WT MEFs grown on coverslips were scratched with a 200-µl pipette tip. Cells were washed and allowed to recover for 4 h before internalization assays. Average pixel intensity from leading to trailing edges within a selected area was calculated using the Plot Profile option in ImageJ. Plot profiles show a representative image of 5–10 cells across three independent experiments.

DAB ablation

10 $\mu g.ml^{-1}$ CTxB-HRP was added to cell monolayers for 2 min at 37°C. Cells were then incubated with 10 $mg.ml^{-1}$ DAB, 50 µM AA in DME for 2 min before incubation with 10 $mg.ml^{-1}$ DAB, 50 µM AA, 0.012% H_2O_2 in DME for a further 2 min. Cells were washed five times with DME before incubation in normal growth media for 4 h. CTxB-555, Tf-647, and anti-CD44 antibodies were then directly added to cells for 2 min before acid stripping, fixation, permeabilization, and labeling for anti-CD44 antibodies. For quantitation of distance migrated, monolayers were imaged after DAB inactivation (time zero) and again after 4 h. Distance between front edges of monolayers on both sides of the wound was measured using Adobe Photoshop CS2. Anti-CD44-HRP and Tf-HRP failed to inhibit either clathrin-independent or -dependent endocytosis at concentrations of 10–100 $\mu g.ml^{-1}$ as used at early times in this assay.

Online supplemental material

Fig. S1 shows that wortmannin treatment of MEFs inhibits the fusion of CLICs with early endosomes, leading to a threefold increase in the number of CLICs per cell. Wortmannin treatment does not noticeably affect the protein profiles of the CLIC-enriched fraction. Fig. S2 shows the consistent nature of membrane profiles in the CLIC-enriched fraction and that CTxB-HRP labels a majority of these profiles when added to cells before the fractionation. Fig. S3 shows the localization of dynamin to CLICs after wortmannin treatment by immunofluorescence and by ultrastructure. Dynamin also labels the neck of profiles in the CLIC-enriched fraction. Video 1 shows the tilt series of CTxB-HRP–laden CLICs after 15 s of internalization. Table S1 lists all the peptides identified from fraction 2.8 with two or more 99% confidence hits from the LC-MS/MS. Online supplemental material is available at http://www.jcb.org/cgi/content/full/jcb.201002119/DC1.

The Institute for Molecular Bioscience is a Special Research Centre of the Australian Research Council. Confocal microscopy was performed at the Australian Cancer Research Foundation (ACRF)/Institute for Molecular Bioscience Dynamic Imaging Facility for Cancer Biology, which was established with the support of the ACRF. The authors acknowledge the facilities as well as scientific and technical assistance from staff in the Australian Microscopy and Microanalysis Facility (AMMRF) at the Centre for Microscopy and Microanalysis at The University of Queensland. We thank Jean Gruenberg for critical appraisal of the manuscript.

This work was supported by grants from the National Health and Medical Research Council of Australia (511005; R.G. Parton and J.F. Hancock) and the Human Frontier Science Program.

Submitted: 22 February 2010
Accepted: 26 July 2010

Published August 16, 2010

References

Bernatchez, P.N., L. Acevedo, C. Fernandez-Hernando, T. Murata, C. Chalouni, J. Kim, H. Erdjument-Bromage, V. Shah, J.P. Gratton, E.M. McNally, et al. 2007. Myoferlin regulates vascular endothelial growth factor receptor-2 stability and function. *J. Biol. Chem.* 282:30745–30753. doi:10.1074/jbc.M704798200

Bretscher, A., D. Reczek, and M. Berryman. 1997. Ezrin: a protein requiring conformational activation to link microfilaments to the plasma membrane in the assembly of cell surface structures. *J. Cell Sci.* 110:3011–3018.

Chadda, R., M.T. Howes, S.J. Plowman, J.F. Hancock, R.G. Parton, and S. Mayor. 2007. Cholesterol-sensitive Cdc42 activation regulates actin polymerization for endocytosis via the GEEC pathway. *Traffic.* 8:702–717. doi:10.1111/j.1600-0854.2007.00565.x

Cheng, Z.J., R.D. Singh, D.K. Sharma, E.L. Holicky, K. Hanada, D.L. Marks, and R.E. Pagano. 2006. Distinct mechanisms of clathrin-independent endocytosis have unique sphingolipid requirements. *Mol. Biol. Cell.* 17:3197–3210. doi:10.1091/mbc.E05-12-1101

Conner, S.D., and S.L. Schmid. 2003. Regulated portals of entry into the cell. *Nature.* 422:37–44. doi:10.1038/nature01451

Cupers, P., A. Veithen, A. Kiss, P. Baudhuin, and P.J. Courtoy. 1994. Clathrin polymerization is not required for bulk-phase endocytosis in rat fetal fibroblasts. *J. Cell Biol.* 127:725–735. doi:10.1083/jcb.127.3.725

Damke, H., T. Baba, D.E. Warnock, and S.L. Schmid. 1994. Induction of mutant dynamin specifically blocks endocytic coated vesicle formation. *J. Cell Biol.* 127:915–934. doi:10.1083/jcb.127.4.915

Damke, H., T. Baba, A.M. van der Bliek, and S.L. Schmid. 1995. Clathrin-independent pinocytosis is induced in cells overexpressing a temperature-sensitive mutant of dynamin. *J. Cell Biol.* 131:69–80. doi:10.1083/jcb.131.1.69

Davis, D.B., A.J. Delmonte, C.T. Ly, and E.M. McNally. 2000. Myoferlin, a candidate gene and potential modifier of muscular dystrophy. *Hum. Mol. Genet.* 9:217–226. doi:10.1093/hmg/9.2.217

Doherty, G.J., and H.T. McMahon. 2009. Mechanisms of endocytosis. *Annu. Rev. Biochem.* 78:857–902. doi:10.1146/annurev.biochem.78.081307.110540

Etienne-Manneville, S. 2004. Cdc42—the centre of polarity. *J. Cell Sci.* 117:1291–1300. doi:10.1242/jcs.01115

Etienne-Manneville, S., and A. Hall. 2001. Integrin-mediated activation of Cdc42 controls cell polarity in migrating astrocytes through PKCzeta. *Cell.* 106:489–498. doi:10.1016/S0092-8674(01)00471-8

Feral, C.C., N. Nishiya, C.A. Fenczik, H. Stuhlmann, M. Slepak, and M.H. Ginsberg. 2005. CD98hc (SLC3A2) mediates integrin signaling. *Proc. Natl. Acad. Sci. USA.* 102:355–360. doi:10.1073/pnas.0404852102

Furtak, V., F. Hatcher, and J. Ochieng. 2001. Galectin-3 mediates the endocytosis of beta-1 integrins by breast carcinoma cells. *Biochem. Biophys. Res. Commun.* 289:845–850. doi:10.1006/bbrc.2001.6064

Gauthier, N.C., P. Monzo, T. Gonzalez, A. Doye, A. Oldani, P. Gounon, V. Ricci, M. Cormont, and P. Boquet. 2007. Early endosomes associated with dynamic F-actin structures are required for late trafficking of H. pylori VacA toxin. *J. Cell Biol.* 177:343–354. doi:10.1083/jcb.200609061

Gauthier, N.C., O.M. Rossier, A. Mathur, J.C. Hone, and M.P. Sheetz. 2009. Plasma membrane area increases with spread area by exocytosis of a GPI-anchored protein compartment. *Mol. Biol. Cell.* 20:3261–3272. doi:10.1091/mbc.E09-01-0071

Glebov, O.O., N.A. Bright, and B.J. Nichols. 2006. Flotillin-1 defines a clathrin-independent endocytic pathway in mammalian cells. *Nat. Cell Biol.* 8:46–54. doi:10.1038/ncb1342

Grande-García, A., A. Echarri, J. de Rooij, N.B. Alderson, C.M. Waterman-Storer, J.M. Valdivielso, and M.A. del Pozo. 2007. Caveolin-1 regulates cell polarization and directional migration through Src kinase and Rho GTPases. *J. Cell Biol.* 177:683–694. doi:10.1083/jcb.200701006

Griffiths, G., R. Back, and M. Marsh. 1989. A quantitative analysis of the endocytic pathway in baby hamster kidney cells. *J. Cell Biol.* 109:2703–2720. doi:10.1083/jcb.109.6.2703

Hansen, C.G., and B.J. Nichols. 2009. Molecular mechanisms of clathrin-independent endocytosis. *J. Cell Sci.* 122:1713–1721. doi:10.1242/jcs.033951

Henley, J.R., E.W. Krueger, B.J. Oswald, and M.A. McNiven. 1998. Dynamin-mediated internalization of caveolae. *J. Cell Biol.* 141:85–99. doi:10.1083/jcb.141.1.85

Hernández-Deviez, D.J., M.T. Howes, S.H. Laval, K. Bushby, J.F. Hancock, and R.G. Parton. 2008. Caveolin regulates endocytosis of the muscle repair protein, dysferlin. *J. Biol. Chem.* 283:6476–6488. doi:10.1074/jbc.M708776200

Huang, Y., S.H. Laval, A. van Remoortere, J. Baudier, C. Benaud, L.V. Anderson, V. Straub, A. Deelder, R.R. Frants, J.T. den Dunnen, et al. 2007. AHNAK, a novel component of the dysferlin protein complex, redistributes to the cytoplasm with dysferlin during skeletal muscle regeneration. *FASEB J.* 21:732–742. doi:10.1096/fj.06-6628com

Idone, V., C. Tam, and N.W. Andrews. 2008a. Two-way traffic on the road to plasma membrane repair. *Trends Cell Biol.* 18:552–559. doi:10.1016/j.tcb.2008.09.001

Idone, V., C. Tam, J.W. Goss, D. Toomre, M. Pypaert, and N.W. Andrews. 2008b. Repair of injured plasma membrane by rapid Ca2+-dependent endocytosis. *J. Cell Biol.* 180:905–914. doi:10.1083/jcb.200708010

Johnson, D.I., and J.R. Pringle. 1990. Molecular characterization of CDC42, a Saccharomyces cerevisiae gene involved in the development of cell polarity. *J. Cell Biol.* 111:143–152. doi:10.1083/jcb.111.1.143

Kalia, M., S. Kumari, R. Chadda, M.M. Hill, R.G. Parton, and S. Mayor. 2006. Arf6-independent GPI-anchored protein-enriched early endosomal compartments fuse with sorting endosomes via a Rab5/phosphatidylinositol-3′-kinase-dependent machinery. *Mol. Biol. Cell.* 17:3689–3704. doi:10.1091/mbc.E05-10-0980

Kirkham, M., A. Fujita, R. Chadda, S.J. Nixon, T.V. Kurzchalia, D.K. Sharma, R.E. Pagano, J.F. Hancock, S. Mayor, and R.G. Parton. 2005. Ultrastructural identification of uncoated caveolin-independent early endocytic vehicles. *J. Cell Biol.* 168:465–476. doi:10.1083/jcb.200407078

Kumari, S., and S. Mayor. 2008. ARF1 is directly involved in dynamin-independent endocytosis. *Nat. Cell Biol.* 10:30–41. doi:10.1038/ncb1666

Lamaze, C., A. Dujeancourt, T. Baba, C.G. Lo, A. Benmerah, and A. Dautry-Varsat. 2001. Interleukin 2 receptors and detergent-resistant membrane domains define a clathrin-independent endocytic pathway. *Mol. Cell.* 7:661–671. doi:10.1016/S1097-2765(01)00212-X

Le, P.U., and I.R. Nabi. 2003. Distinct caveolae-mediated endocytic pathways target the Golgi apparatus and the endoplasmic reticulum. *J. Cell Sci.* 116:1059–1071. doi:10.1242/jcs.00327

Lee, J.L., M.J. Wang, P.R. Sudhir, and J.Y. Chen. 2008. CD44 engagement promotes matrix-derived survival through the CD44-SRC-integrin axis in lipid rafts. *Mol. Cell. Biol.* 28:5710–5723. doi:10.1128/MCB.00186-08

Legg, J.W., C.A. Lewis, M. Parsons, T. Ng, and C.M. Isacke. 2002. A novel PKC-regulated mechanism controls CD44 ezrin association and directional cell motility. *Nat. Cell Biol.* 4:399–407. doi:10.1038/ncb797

Lundmark, R., G.J. Doherty, M.T. Howes, K. Cortese, Y. Vallis, R.G. Parton, and H.T. McMahon. 2008. The GTPase-activating protein GRAF1 regulates the CLIC/GEEC endocytic pathway. *Curr. Biol.* 18:1802–1808. doi:10.1016/j.cub.2008.10.044

Mayor, S., and R.E. Pagano. 2007. Pathways of clathrin-independent endocytosis. *Nat. Rev. Mol. Cell Biol.* 8:603–612. doi:10.1038/nrm2216

Montesano, R., J. Roth, A. Robert, and L. Orci. 1982. Non-coated membrane invaginations are involved in binding and internalization of cholera and tetanus toxins. *Nature.* 296:651–653. doi:10.1038/296651a0

Mrass, P., I. Kinjyo, L.G. Ng, S.L. Reiner, E. Puré, and W. Weninger. 2008. CD44 mediates successful interstitial navigation by killer T cells and enables efficient antitumor immunity. *Immunity.* 29:971–985. doi:10.1016/j.immuni.2008.10.015

Murk, J.L., G. Posthuma, A.J. Koster, H.J. Geuze, A.J. Verkleij, M.J. Kleijmeer, and B.M. Humbel. 2003. Influence of aldehyde fixation on the morphology of endosomes and lysosomes: quantitative analysis and electron tomography. *J. Microsc.* 212:81–90. doi:10.1046/j.1365-2818.2003.01238.x

Nishimura, T., and K. Kaibuchi. 2007. Numb controls integrin endocytosis for directional cell migration with aPKC and PAR-3. *Dev. Cell.* 13:15–28. doi:10.1016/j.devcel.2007.05.003

Palamidessi, A., E. Frittoli, M. Garré, M. Faretta, M. Mione, I. Testa, A. Diaspro, L. Lanzetti, G. Scita, and P.P. Di Fiore. 2008. Endocytic trafficking of Rac is required for the spatial restriction of signaling in cell migration. *Cell.* 134:135–147. doi:10.1016/j.cell.2008.05.034

Parton, R.G., and K. Simons. 2007. The multiple faces of caveolae. *Nat. Rev. Mol. Cell Biol.* 8:185–194. doi:10.1038/nrm2122

Parton, R.G., B. Joggerst, and K. Simons. 1994. Regulated internalization of caveolae. *J. Cell Biol.* 127:1199–1215. doi:10.1083/jcb.127.5.1199

Pelkmans, L., D. Püntener, and A. Helenius. 2002. Local actin polymerization and dynamin recruitment in SV40-induced internalization of caveolae. *Science.* 296:535–539. doi:10.1126/science.1069784

Radhakrishna, H., and J.G. Donaldson. 1997. ADP-ribosylation factor 6 regulates a novel plasma membrane recycling pathway. *J. Cell Biol.* 139:49–61. doi:10.1083/jcb.139.1.49

Rege, T.A., M.A. Pallero, C. Gomez, H.E. Grenett, J.E. Murphy-Ullrich, and J.S. Hagood. 2006. Thy-1, via its GPI anchor, modulates Src family kinase and focal adhesion kinase phosphorylation and subcellular localization, and fibroblast migration, in response to thrombospondin-1/hep I. *Exp. Cell Res.* 312:3752–3767. doi:10.1016/j.yexcr.2006.07.029

Ricci, V., A. Galmiche, A. Doye, V. Necchi, E. Solcia, and P. Boquet. 2000. High cell sensitivity to *Helicobacter pylori* VacA toxin depends on a GPI-anchored protein and is not blocked by inhibition of the clathrin-mediated pathway of endocytosis. *Mol. Biol. Cell.* 11:3897–3909.

Richter, T., M. Floetenmeyer, C. Ferguson, J. Galea, J. Goh, M.R. Lindsay, G.P. Morgan, B.J. Marsh, and R.G. Parton. 2008. High-resolution 3D quantitative analysis of caveolar ultrastructure and caveola-cytoskeleton interactions. *Traffic.* 9:893–909. doi:10.1111/j.1600-0854.2008.00733.x

Römer, W., L. Berland, V. Chambon, K. Gaus, B. Windschiegl, D. Tenza, M.R. Aly, V. Fraisier, J.C. Florent, D. Perrais, et al. 2007. Shiga toxin induces tubular membrane invaginations for its uptake into cells. *Nature.* 450:670–675. doi:10.1038/nature05996

Sabharanjak, S., P. Sharma, R.G. Parton, and S. Mayor. 2002. GPI-anchored proteins are delivered to recycling endosomes via a distinct cdc42-regulated, clathrin-independent pinocytic pathway. *Dev. Cell.* 2:411–423. doi:10.1016/S1534-5807(02)00145-4

Sandvig, K., and B. van Deurs. 1994. Endocytosis and intracellular sorting of ricin and Shiga toxin. *FEBS Lett.* 346:99–102. doi:10.1016/0014-5793(94)00281-9

Sandvig, K., S. Olsnes, O.W. Petersen, and B. van Deurs. 1987. Acidification of the cytosol inhibits endocytosis from coated pits. *J. Cell Biol.* 105:679–689. doi:10.1083/jcb.105.2.679

Shimonaka, M., K. Katagiri, T. Nakayama, N. Fujita, T. Tsuruo, O. Yoshie, and T. Kinashi. 2003. Rap1 translates chemokine signals to integrin activation, cell polarization, and motility across vascular endothelium under flow. *J. Cell Biol.* 161:417–427. doi:10.1083/jcb.200301133

Sigismund, S., E. Argenzio, D. Tosoni, E. Cavallaro, S. Polo, and P.P. Di Fiore. 2008. Clathrin-mediated internalization is essential for sustained EGFR signaling but dispensable for degradation. *Dev. Cell.* 15:209–219. doi:10.1016/j.devcel.2008.06.012

Simpson, K.J., L.M. Selfors, J. Bui, A. Reynolds, D. Leake, A. Khvorova, and J.S. Brugge. 2008. Identification of genes that regulate epithelial cell migration using an siRNA screening approach. *Nat. Cell Biol.* 10:1027–1038. doi:10.1038/ncb1762

Suga, K., K. Katagiri, T. Kinashi, M. Harazaki, T. Iizuka, M. Hattori, and N. Minato. 2001. CD98 induces LFA-1-mediated cell adhesion in lymphoid cells via activation of Rap1. *FEBS Lett.* 489:249–253. doi:10.1016/S0014-5793(00)02222-5

Torgersen, M.L., G. Skretting, B. van Deurs, and K. Sandvig. 2001. Internalization of cholera toxin by different endocytic mechanisms. *J. Cell Sci.* 114:3737–3747.

Vassilieva, E.V., K. Gerner-Smidt, A.I. Ivanov, and A. Nusrat. 2008. Lipid rafts mediate internalization of beta1-integrin in migrating intestinal epithelial cells. *Am. J. Physiol. Gastrointest. Liver Physiol.* 295:G965–G976. doi:10.1152/ajpgi.00082.2008

Weibel, E.R. 1979. Stereological Methods. 1. Practical methods for biological morphometry. Academic Press Inc., New York.

Yarar, D., C.M. Waterman-Storer, and S.L. Schmid. 2007. SNX9 couples actin assembly to phosphoinositide signals and is required for membrane remodeling during endocytosis. *Dev. Cell.* 13:43–56. doi:10.1016/j.devcel.2007.04.014

Published August 16, 2010

Howes et al., http://www.jcb.org/cgi/content/full/jcb.201002119/DC1

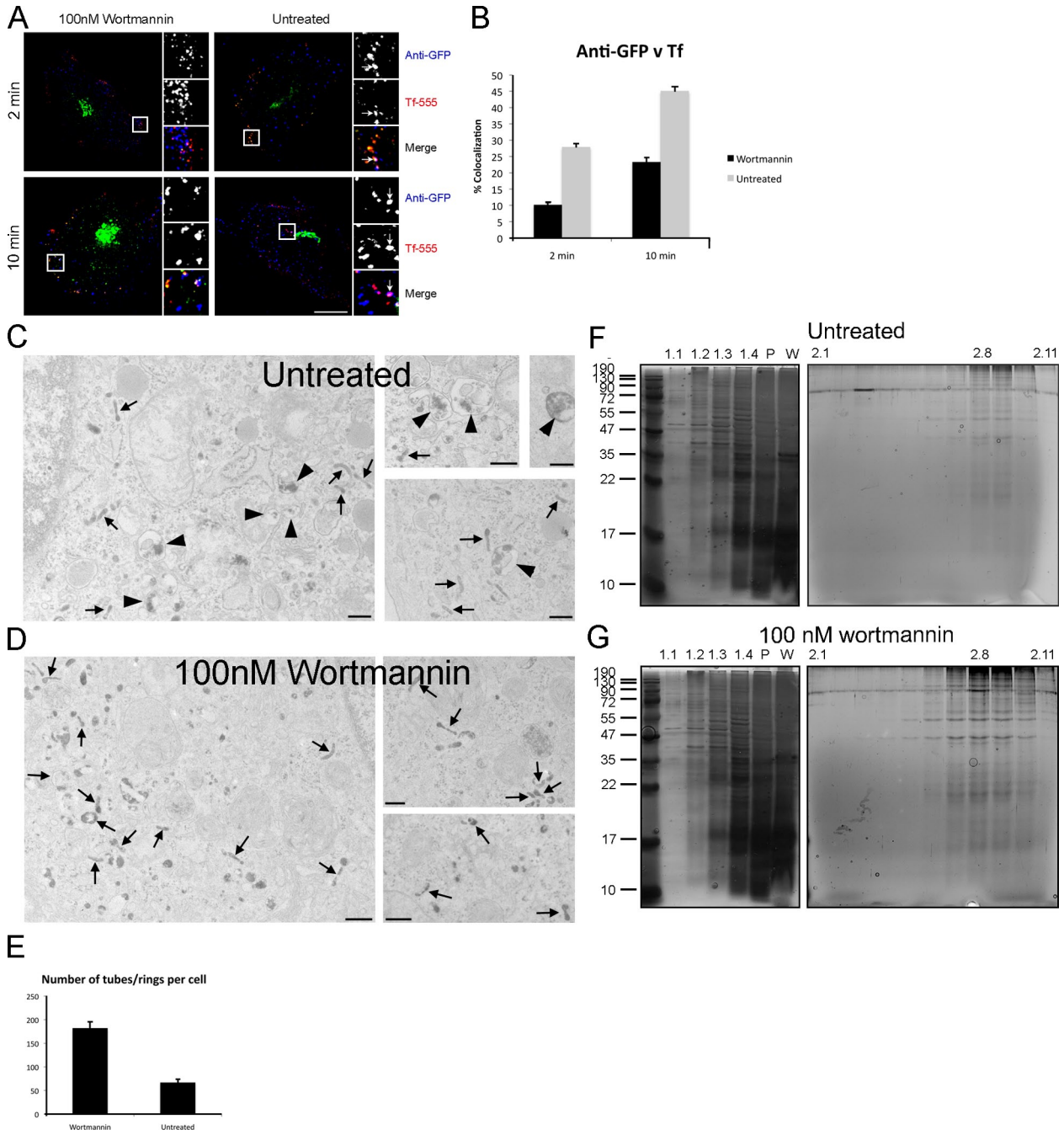

Figure S1. **Inhibition of CLIC maturation through wortmannin treatment.** (A) 3T3-GPI cells treated or not with 100 nM wortmannin were incubated with anti-GFP antibodies and Tf-546 for 2 or 10 min at 37°C. Arrows indicate points of colocalization. (B) 10–12 cells across three independent experiments from A were processed for colocalization using Volocity v3.7. WT MEFs were treated with DMSO (C) or with 100 nM wortmannin (D) and were then pulsed with CTxB-HRP for 10 min. DAB reaction was performed with AA before fixation. Arrows indicate tubular and ring-shaped CLICs. Arrowheads show early endosomes. Bars, 200 nm. (E) Quantitation of HRP-positive rings and tubules across 4–6 cells in two independent experiments treated as in C or D. Error bars show SEM. (F and G) Silver-stained polyacrylimide gels of fractions from cells left untreated (F) or treated with 100 nM wortmannin (G). The major protein bands in Fraction 2.8 are consistent across samples. More protein is visible in wortmannin-treated samples consistent with an increase in the number of CLICs in this pool. One band in particular shifts from a significant pool in Fraction 2.3 to Fraction 2.8 after wortmannin treatment. By Western blot this band corresponds to the internalized anti-GFP antibody (not depicted). As anti-GFP labels multiple compartments in untreated control cells (C), this shift represents the specific concentration in CLICs after wortmannin treatment.

Published August 16, 2010

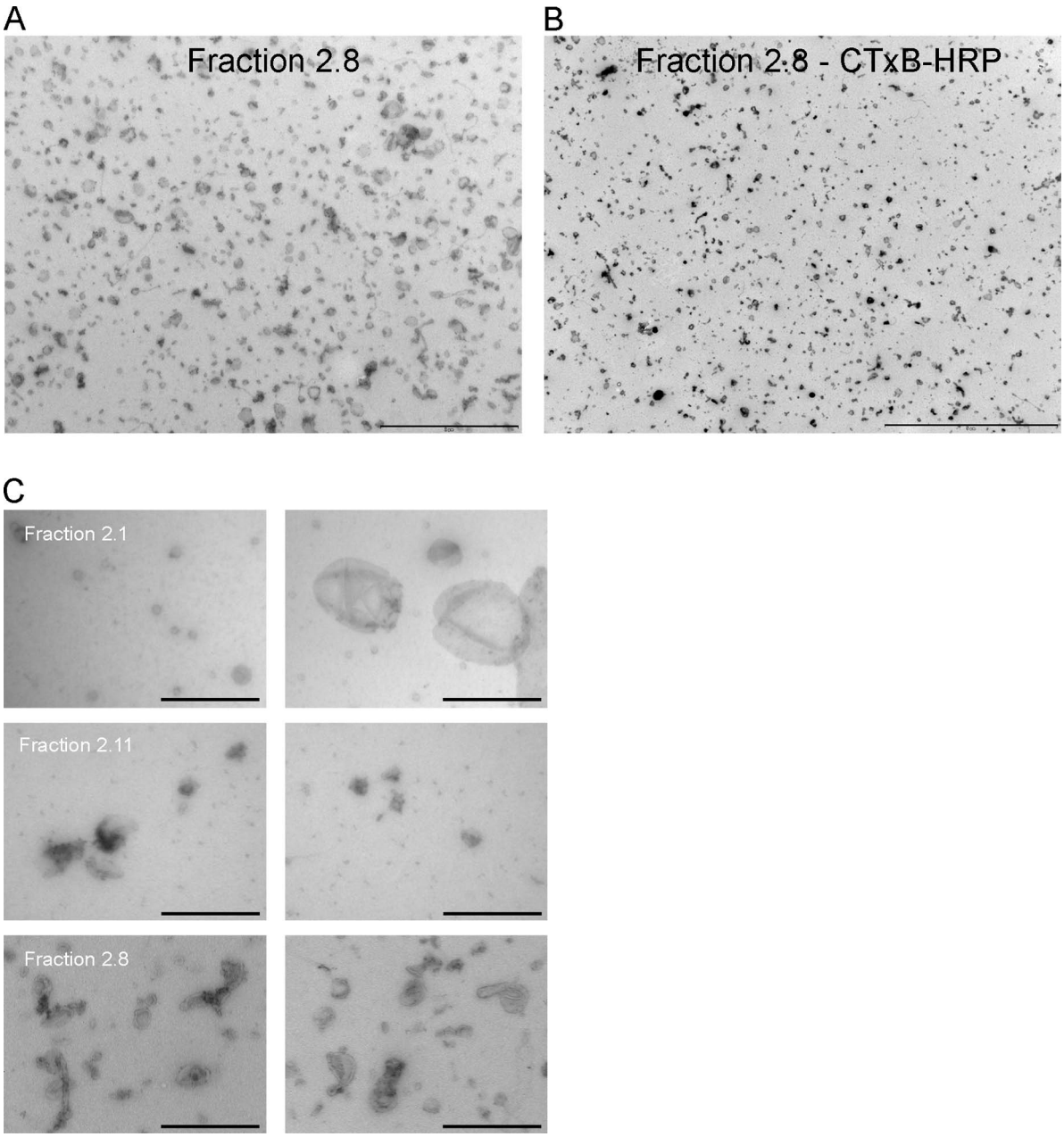

Figure S2. **Membrane profiles of fractions from Nycodenz gradient.** (A) Adsorbed and glutaraldehyde-fixed samples from Fraction 2.8 were visualized by EM. The morphology of structures within this fraction shows a highly enriched but not pure concentration of structures that have the striking morphology of CLICs. Although these structures range from 100–300 nm in diameter they display a consistent ring-shaped morphology, with some tubular extensions. Smaller microsomes are present but not predominant within this fraction. Bar, 2 µm. (B) CTxB-HRP–internalized NIH3T3s were subjected to the isolation protocol. DAB reaction was performed on fixed and adsorbed samples from Fraction 2.8. Low magnification image shows the vast bulk of membrane within this fraction is positive for internalized CTxB, shown as electron-dense structures. Stereology on 20 randomly selected fields calculates that 70.0% of membrane within this fraction is positive for CTxB-HRP. (C) Fractions 2.1 and 2.11 were fixed and adsorbed onto a 100 mesh copper grid. Representative images from these fractions are shown and compared with the structures found in Fraction 2.8. Bars, 500 nm.

Published August 16, 2010

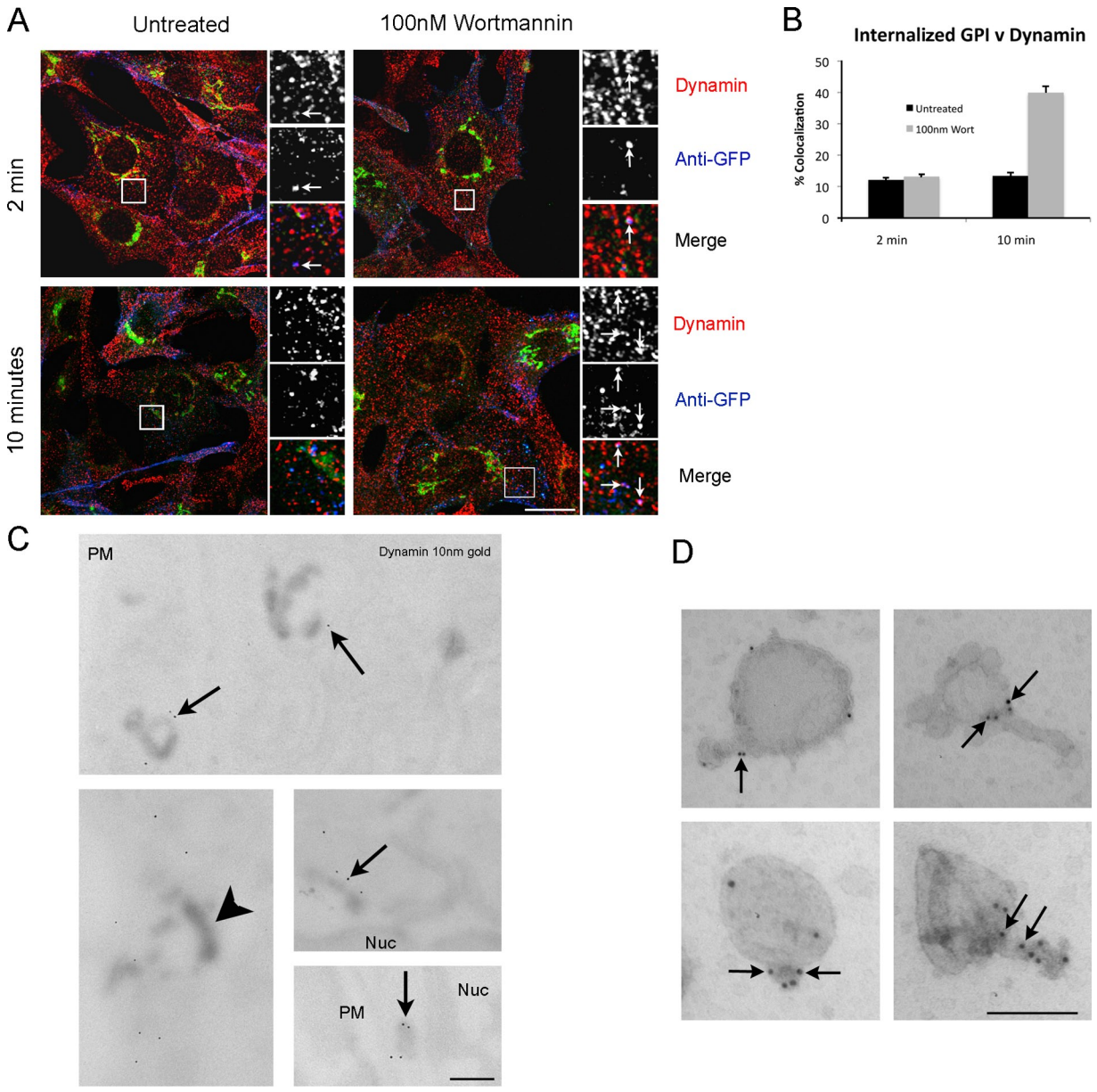

Figure S3. **Dynamin localizes to maturing CLICs.** (A) 3T3-GPI cells were treated for 20 min with 100 nM wortmannin or were left untreated before internalization of anti-GFP antibodies for 2 or 10 min at 37°C. Cells were placed on ice and acid stripped to remove surface anti-GFP labeling before fixation and labeling for endogenous dynamin. Merged images of selected areas are shown. Arrows show structures in which dynamin and anti-GFP colocalize. Bar, 10 µm. (B) 10–12 cells across two independent experiments treated as in A were imaged and colocalization between anti-GFP and dynamin was calculated. Error bars show SEM. (C) NIH3T3 cells were treated with 100 nM wortmannin for 20 min before internalization of CTxB-HRP for 5 min. Cells were placed on ice and processed for the DAB reaction. Cells were fixed for Tokuyasu cryosection. Dynamin-labeled sections were not stained with uranyl acetate but were layered with a film of 2% methyl cellulose. Arrows show labeling on electron-dense, CTxB-HRP–positive structures. Arrowhead shows a nonlabeled CTxB-HRP–positive structure. PM, plasma membrane; Nuc, nucleus. Bar, 200 nm. (D) High magnification images of dynamin labeling on structures in Fraction 2.8. Numerous structures show dynamin localization at the neck of tubular extensions. Bar. 200 nm.

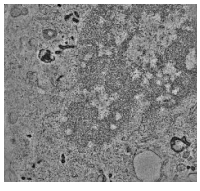

Video 1. **Tomogram of CTxB-HRP–laden CLICs.** CTxB-HRP was bound to WT MEFs on ice for 20 min. Cells were warmed to 37°C in 5% CO_2 for 15 s before being placed back on ice in ice-cold PBS. DAB reaction was performed on ice, fixed in 2.5% glutaraldehyde, and processed for tomography as described in Materials and methods. Each frame of the movie represents a 1° increment in tilt angle.

Published August 16, 2010

Table S1. **All peptides with two or more 99% confident hits**

Peptide	Location	Function	Accession
4F2 cell-surface antigen heavy chain/CD98	PM	Receptor	P10852|4F2_MOUSE
78-kD glucose-regulated protein	PM/ER	Chaperone	P20029|GRP78_MOUSE
Actin, cytoplasmic 1	Cytosol	Cytoskeleton	P63260|ACTG_MOUSE
Alpha-2-HS-glycoprotein/Fetuin	PM/Endosomes	Receptor	P29699|FETUA_MOUSE
Annexin A2	Endosomes	Membrane homeostasis	P07356|ANXA2_MOUSE
B cell receptor-associated protein 31	PM	Receptor	Q61335|BAP31_MOUSE
Calcium-binding protein p22	PM/ER	Receptor	P61022|CHP1_MOUSE
Calmodulin	PM/Endosomes/ER	Chaperone	P62204|CALM_MOUSE
Calnexin	ER	Chaperone	P35564|CALX_MOUSE
Calreticulin	ER	Chaperone	P14211|CALR_MOUSE
Calumenin	ER	Chaperone	O35887|CALU_MOUSE
Cathepsin L	Endosomes	Enzyme	Q6LAF5|Q6LAF5_MOUSE
Cation-dependent mannose-6-phosphate receptor	PM/Endosomes	Receptor	P24668|MPRD_MOUSE
Caveolin-1	PM	Membrane homeostasis	P49817|CAV1_MOUSE
CD109 antigen	PM	Receptor	
CD44 antigen	PM	Adhesion	P15379|CD44_MOUSE
Collagen alpha-2(I)	ECM	Miscellaneous	Q01149|CO1A2_MOUSE
Collectin-12	PM	Receptor	Q8K4Q8|COL12_MOUSE
Cytoskeleton-associated protein 4	PM/Endosomes	Adhesion	Q8BMK4|CKAP4_MOUSE
Endoplasmic reticulum protein ERp29	ER	Enzyme	P57759|ERP29_MOUSE
Endoplasmin	ER	Chaperone	P08113|ENPL_MOUSE
ERGIC-53	ER/Golgi	Membrane homeostasis	Q9D0F3|LMAN1_MOUSE
FAM3C	ER	Unknown	Q91VU0|FAM3C_MOUSE
FK506-binding protein 2 precursor	PM/ER	Chaperone	P45878|FKBP2_MOUSE
Fructose-bisphosphate aldolase A	Cytosol/Endosomes	Enzyme	P05064|ALDOA_MOUSE
Galectin-3	PM	Adhesion	P16110|LEG3_MOUSE
Glyceraldehyde-3-phosphate dehydrogenase	Cytosol	Enzyme	P16858|G3P_MOUSE
Golgi apparatus protein 1/MG-160	PM/Golgi	Receptor	Q61543|GSLG1_MOUSE
Guanine nucleotide-binding protein G(o)	PM	Signalling	P18872|GNAO1_MOUSE
Heat shock cognate 71 kD	Cytosol	Chaperone	P63017|HSP7C_MOUSE
Integrin beta-1	PM	Adhesion	P09055|ITB1_MOUSE
Leucine-rich repeat-containing protein 59	PM	Unknown	Q922Q8|LRC59_MOUSE
Lysosome-associated membrane glycoprotein 2	Endosomes	Membrane homeostasis	P17047|LAMP2_MOUSE
Lysozyme C type P	Endosomes	Enzyme	P17897|LYSCP_MOUSE
Membrane-associated progesterone receptor component 1	PM/ER	Receptor	O55022|PGRC1_MOUSE
Moesin	PM	Adhesion	P26041|MOES_MOUSE
Myoferlin (Fer-1-like protein 3)	PM	Membrane homeostasis	Q69ZN7|MYOF_MOUSE
NADPH-cytochrome P450 reductase	Cytosol	Chaperone	P37040|NCPR_MOUSE
Neuroblast differentiation-associated protein AHNAK	PM	Membrane homeostasis	Q8VDN3|Q8VDN3_MOUSE
Neutral alpha-glucosidase	PM/Endosomes	Enzyme	Q8BHN3|GANAB_MOUSE
Nicastrin	TGN	Miscellaneous	P57716|NICA_MOUSE
Nucleobindin-1	ER	Membrane homeostasis	Q02819|NUCB1_MOUSE
Peptidyl-prolyl cis-trans isomerase C	Cytosol	Enzyme	P30412|PPIC_MOUSE
Predicted	Unknown	Unknown	Q80VP7|Q80VP7_MOUSE
Progesterone receptor membrane component 1	PM/Endosomes	Membrane homeostasis	O55022|PGRC1_MOUSE
Prolow-density lipoprotein receptor-related protein 1	PM	Receptor	Q91ZX7|LRP1_MOUSE
Prosaposin	PM/Endosomes	Enzyme	Q61207|SAP_MOUSE
Prostaglandin-endoperoxide synthase 1	PM/ER	Enzyme	P22437|PGH1_MOUSE
Protein disulfide-isomerase A3	ER	Chaperone	P27773|PDIA3_MOUSE
Protein-lysine 6-oxidase	Cytosol	Enzyme	P28301|LYOX_MOUSE
Ras-related C3 botulinum toxin substrate 1	PM/Endosomes	GTPase	P63001|RAC1_MOUSE
Ras-related protein Rab-11A	Endosomes	GTPase	P62492|RB11A_MOUSE
Ras-related protein Rab-14	Endosomes	GTPase	Q91V41|RAB14_MOUSE
Ras-related protein Rab-18	ER	GTPase	P35293|RAB18_MOUSE
Ras-related protein Rab-1A	PM/Endosomes	GTPase	P62821|RAB1A_MOUSE
Ras-related protein Rab-2A	ER	GTPase	P53994|RAB2A_MOUSE

Published August 16, 2010

Table S1. **All peptides with two or more 99% confident hits** *(Continued)*

Peptide	Location	Function	Accession
Ras-related protein Rab-5A	Endosomes	GTPase	Q9CQD1|RAB5A_MOUSE
Ras-related protein Rab-6B	PM/Endosomes	GTPase	P61294|RAB6B_MOUSE
Ras-related protein Rab-7a	Endosomes	GTPase	P51150|RAB7A_MOUSE
Ras-related protein Rap-1b	PM	GTPase	Q99JI6|RAP1B_MOUSE
Receptor expression-enhancing protein 5	PM	Membrane homeostasis	Q60870|REEP5_MOUSE
Reticulon-4	PM/ER	Membrane homeostasis	Q99P72|RTN4_MOUSE
RIKEN cDNA 4732456N10 gene	Unknown	Unknown	Q148Q7|Q148Q7_MOUSE
Serpin H1 precursor	Cytosol	Chaperone	P19324|SERPH_MOUSE
Serum albumin	Serum	Miscellaneous	P07724|ALBU_MOUSE
Spectrin	Cytosol	Cytoskeleton	P08032|SPTA1_MOUSE
Sterol-4-alpha-carboxylate 3-dehydrogenase	PM/ER	Enzyme	Q9R1J0|NSDHL_MOUSE
Striatin-3	ER	Enzyme	Q9ERG2|STRN3_MOUSE
T-complex protein 1 subunit gamma	ER	Chaperone	P80318|TCPG_MOUSE
Thioredoxin domain-containing protein 4	ER	Enzyme	Q9D1Q6|TXND4_MOUSE
Thy-1 membrane glycoprotein	PM	Adhesion	P01831|THY1_MOUSE
Transgelin-2	Cytosol	Enzyme	Q9WVA4|TAGL2_MOUSE
Transmembrane emp24 domain-containing protein 10	PM/ER	Receptor	Q9D1D4|TMEDA_MOUSE
Transmembrane emp24 domain-containing protein 2	ER	Receptor	Q9R0Q3|TMED2_MOUSE
Transmembrane emp24 domain-containing protein 9	ER	Receptor	Q99KF1|TMED9_MOUSE
Transmembrane protein 33	PM/ER	Unknown	Q9CR67|TMM33_MOUSE
Tubulin alpha-1A	Cytosol	Cytoskeleton	P68369|TBA1A_MOUSE
Vesicle-associated membrane protein-associated protein B	PM/ER	Membrane homeostasis	Q9QY76|VAPB_MOUSE
Vesicle-trafficking protein SEC22b	COP-coated vesicles	Membrane homeostasis	O08547|SC22B_MOUSE
Vimentin	Cytosol	Cytoskeleton/Adhesion	P20152|VIME_MOUSE

Full list of CLIC candidate proteins. All targets with two or more 99% confident peptide identifications. Primary localization and function are shown. ECM, extracellular matrix; ER, endoplasmic reticulum; PM, plasma membrane; TGN, trans-Golgi network.